Robustness Analysis of Hypersonic Vehicle Controllers

Colby McGinley

A thesis submitted in partial fulfillment of the
requirements for the degree of

Master of Science in Aeronautics & Astronautics

University of Washington

2018

Committee:

Eli Livne, Chair

Kristi Morgansen

Program Authorized to Offer Degree:
Aeronautics and Astronautics

©Copyright 2018
Colby McGinley

In presenting this thesis in partial fulfillment of the requirements for a masters degree at the University of Washington, I agree that the Library shall make its copies freely available for inspection. I further agree that extensive copying of this thesis is allowable only for scholarly purposes, consistent with the "fair use" as prescribed in the U.S. Copyright Law. Any other reproduction for any purposes or by any means shall not be allowed without my written permission.

The views expressed are those of the author and do not reflect the official policy or position of the US Air Force, Department of Defense or the US Government.

University of Washington

Abstract

Robustness Analysis of Hypersonic Vehicle Controllers

Colby McGinley

Chair of the Supervisory Committee:
Professor Eli Livne
Aeronautics and Astronautics

Air-breathing hypersonic vehicles, when fully developed, will offer travel in the atmosphere at unprecedented speeds. Capturing their physical behavior by analytical / numerical models is still a major challenge, still limiting the development of controls technology for such vehicles. To study, in an exploratory manner, active control of air-breathing hypersonic vehicles, an analytical, simplified, model of a generic hypersonic air-breathing vehicle in flight was developed by researchers at the Air Force Research Labs in Dayton, Ohio, along with control laws. Elevator deflection and fuel-to-air ratio were used as inputs. However, that model is very approximate, and the field of hypersonics still faces many unknowns. This thesis contributes to the study of control of air-breathing hypersonic vehicles in a number of ways: First, regarding control laws synthesis, optimal gains are chosen for the previously developed control law alongside an alternate control law modified from existing literature by minimizing the Lyapunov function derivative using Monte Carlo simulation. This is followed by analysis of the robustness of the control laws in the face of system parametric uncertainties using Monte Carlo simulations. The resulting statistical distributions of the commanded response are analyzed, and linear regression is used to determine, via sensitivity analysis, which uncertain parameters have the largest impact on the desired outcome.

TABLE OF CONTENTS

Page

List of Figures . . . iii

List of Tables . . . v

Chapter 1: Introduction . . . 1

Chapter 2: Hypersonic Vehicle Model . . . 4
- 2.1 Truth Model . . . 4
  - 2.1.1 Aerodynamic Forces . . . 5
  - 2.1.2 Propulsion . . . 6
  - 2.1.3 Unsteady Effects . . . 7
  - 2.1.4 Structural Dynamics . . . 8
  - 2.1.5 Equations of Motion . . . 9
  - 2.1.6 Linear Stability Analysis . . . 9

Chapter 3: Controller Design . . . 11
- 3.1 Control Design Model . . . 11
- 3.2 Original Controller . . . 13
  - 3.2.1 Step 1 . . . 15
  - 3.2.2 Step 2 . . . 18
  - 3.2.3 Step 3 . . . 20
- 3.3 New Controller . . . 21

Chapter 4: Stability Analysis and Gain Selection . . . 25
- 4.1 Lyapunov Stability . . . 25
  - 4.1.1 Original Controller Analysis . . . 25

4.2 Max K_1 and K_2 Gains for Original Controller 27
4.3 Monte Carlo Gain Selection 28

Chapter 5: Monte Carlo Analysis 33
5.1 Monte Carlo Methods 33
5.1.1 Input Distributions 34
5.1.2 Statistical Analysis 34
5.2 Model Uncertainty 36
5.2.1 Sources of Uncertainty 37
5.2.2 Atmospheric Uncertainty 37
5.2.3 Propulsion Uncertainty 37
5.2.4 Aerodynamic Uncertainty 39
5.2.5 Structural Uncertainty 39
5.3 Set Up 41
5.4 Results 42
5.4.1 Flight Path Angle Results 42
5.4.2 Mach Number Results 47

Chapter 6: Conclusions 51

Bibliography 52

Appendix A: Control Design Model 54

LIST OF FIGURES

Figure Number Page

2.1 Generalized Hypersonic Vehicle Geometry[1] 5

2.2 Poles and Zeros of Linearized Hypersonic Vehicle Trimmed at M=10 and $\bar{q} = 1500$psf. Poles (Circles) and Zeros (x's) 10

3.1 C_L Curve-Fit over Hypersonic Vehicle Domain[2] 13

3.2 Indirect Manifold Approach[2] 14

3.3 Time Simulation of Closed Loop System with Original Control Design[2] . . . 16

3.4 Comparison of different methods for calculating α_r 19

3.5 Time Simulation of Closed Loop System with Fixed Original Controller . . . 21

3.6 Modified Fiorentini Approach 22

3.7 Time Simulation of Closed Loop System with New Control Design 24

4.1 Max K_2 29

4.2 The elevator input, δ_e, bounces back and forth between its limits. Gains: $K_1 = 0.05$, $K_2 = 0.48$, $K_3 = 4.95$, $K_4 = 9.95$ 30

4.3 How $\dot{V}$ Changes With Each Random Set of Gains (Blue Dots Maintain Negative Definiteness, Red Dots Do Not) 31

4.4 Nominal Trajectory With Optimal Gains 32

5.1 Monte Carlo Method[3] 33

5.2 Flow of Uncertainty in Matlab Model (Red Denotes Uncertain Input Parameters) 40

5.3 Flight Path Angle Trajectories 44

5.4 Probability Distribution of Final Flight Path Angle Under Small Parametric Deviation 45

5.5 Probability Distribution of Final Flight Path Angle Under Large Parametric Deviation 46

5.6 Mach Number Trajectories 48

5.7 Probability Distribution of Final Mach Number Small Parametric Deviation 49
5.8 Probability Distribution of Final Mach Number Large Parametric Deviation 50

LIST OF TABLES

Table Number Page

4.1 Range of Flight Conditions Tested 27
4.2 Gain Ranges 30
4.3 Selected Gains 32

5.1 Uncertain Parameters and Their Distributions. All Standard Deviations are as a Percentage of the Nominal Parameter Value 41
5.2 Final Flight Path Angle Statistics 45
5.3 Percentage of Final γ that Falls within Specified Range from the Nominal Trajectory. Nominal trajectory is trajectory with standard deviation set to zero 46
5.4 Regression Coefficients: 95% Confidence Intervals of Statistically Significant Uncertain Input Parameters Affecting Final Flight Path Angle 47
5.5 Final Mach Statistics 49
5.6 Mach Regression Coefficients: 95% Confidence Intervals of Statistically Significant Uncertain Input Parameters Affecting Final Mach Number 50

A.1 Groupings of Curve-Fit Terms. 54

ACKNOWLEDGMENTS

I would like to thank the Department of Aeronautics and Astronautics at the University of Washington for allowing me to accomplish this goal of mine. The quality of instruction and mentorship I have received will be of incalculable value to me. I would like to thank Professors Kristi Morgansen and Eli Livne for taking me mid-way through my studies at the University of Washington to help me with this thesis. Also, my lab mates have been incredible in both providing support to me as well as good times.

Chapter 1

INTRODUCTION

Air-breathing hypersonic vehicles promise faster transportation, reusable platforms for space launch, or serve for missile propulsion. “Hypersonic” is usually classified as velocities exceeding five times the speed of sound. “Air-breathing” refers to propulsion that takes in oxygen from the air it is flying through to be used for combustion and the production of thrust. This qualifier is what makes air-breathing hypersonic vehicles potentially more efficient means of transportation than rockets. Rockets must carry oxygen onboard, which along with the tanks necessary for its storage, add a significant amount of weight.

Significant challenges still exist in the field of air-breathing hypersonic flight, however. The extremely high velocities produce high drag. This requires careful integration of the engine into the body in order to reduce drag and allow the engine to operate efficiently. Scramjet propulsion (supersonic combusting ramjet) is necessary, as slowing hypersonic air to subsonic speeds before combustion would create too much drag and pressure loss. Unfortunately, scramjet engines only work once the vehicle is moving at high supersonic speeds. Despite these challenges, the U.S. Air Force has built and successfully flight tested two air-breathing hypersonic airplanes. The X-43, tested in 2004, reached and maintained a velocity of Mach 9.6 for over 10 seconds.[4] This was the first successfully flight tested air-breathing hypersonic vehicle. The next successful flight test vehicle was the X-51A Waverider, which flew under scramjet propulsion for over six minutes at speeds reaching Mach 5.1.[5] This test vehicle proved the feasibility of scramjet propulsion with hydrocarbon fuels.

Strong coupling between the aerodynamics, propulsion, and structural dynamics make control strategies and modeling difficult. The first comprehensive analytical hypersonic vehicle model was developed by Chavez and Schmidt.[6] Their work used Newtonian impact theory to approximate the pressure distribution over a very simplified 2-D geometry. The analytical equations for the forces and moments were then linearized to find stability and control flight dynamic derivatives.

In 2006, Bolender and Doman, at the US Air Force Research Labs in Dayton, Ohio, began work on a more complex hypersonic vehicle mathematical model[1] in an effort to create a more realistic "plant" model of a hypersonic vehicle for active control research purposes. Their mathematical model of a 2D hypersonic vehicle used oblique shock theory and Prandtl-Meyer expansion fan theory instead of Newtonian impact theory to calculate the pressure distributions over the vehicle. Flexible body dynamics were also included in their model. This model captures all key complex interactions between the aerothermodynamics, propulsion, and structural dynamics on the complete system dynamics.

Many control synthesis studies in the literature are for linearized versions of hypersonic vehicle models. Such controllers are either for more simplified models that do not consider coupling between the elevator and lift,[7–9] or are configured with a canard to simplify the dynamics.[10, 11] Here, the model under consideration is the more complex model of Doman and Bolender.[1] Additionally, since canards also cause structural issues (the canard can intersect with the bow shock, leading to extreme structural heating), the model of used in this thesis has only elevator deflection and fuel ratio as control effectors used control longitudinal dynamics. The regulated outputs are flight path angle and Mach number.

A controller for such a model was developed by McKenna.[2] This controller deals with the non-minimum phase behavior created by only having an elevator to control the pitch of the vehicle (The non-minimum phase behavior and unstable zero dynamics of the model prevents the use of many control strategies such as dynamic inversion). This controller by McKenna[2] is only a proportional controller designed using a simplified control design model. How well it handles parametric uncertainty in the full fidelity hypersonic vehicle model is unknown.

Note: the term “full fidelity model” is used here for the full complexity 2D model of Bolander and Doman, and the model used by McKenna was a simplified version. It must be remembered that, while capturing the core interdisciplinary interactions involved, the “full fidelity” model here is far from actual full fidelity math models of 3D actual hypersonic vehicles. Uncertainty in the math models of hypersonic vehicles can still be significant and must be addressed by the control designer.

Robust controllers for simplified or linearized hypersonic vehicles have been presented in the literature.[7,11] Such publications typically just state that their controllers can withstand a certain percentage of system model coefficient deviation and they do not include thorough statistical analyses of uncertainty propagation and its effect on controller design and controller performance.

Monte Carlo methods[12] have been used to study the propagation of uncertainty in hypersonic vehicle propulsion systems.[13] However, for the controller by McKenna, no such analysis has been carried out.

In this thesis, the power and generality of Monte Carlo simulation will be used to assess how well the McKenna controller[2] maintains stability and tracks towards its regulated output in the face of system uncertainties. This result will be compared to a modified control law from Fiorentini.[11] In addition the work includes assessing which inputs into the hypersonic vehicle model have, with their uncertainties, the greatest effect on the uncertainty of the outcomes.

The thesis is structured as follows: Chapter 2 describes the hypersonic vehicle math model. Chapter 3 describes both control laws used in this thesis, while Chapter 4 explains how the stability was determined and how control law gains were selected. Monte Carlo robustness analysis is then described step by step, followed by results and discussion.

Chapter 2

HYPERSONIC VEHICLE MODEL

Accurate modeling of the hypersonic vehicle is a major challenge. Even with more advanced modeling techniques, there will always be sources of uncertainty. There are two models that are important in this work. The first is what will be called the Truth Model - a “high fidelity” simulation developed by Michael Bolender and David Doman from the Air Force Research Laboratory at Wright Patterson Air Force Base. The second is the Control Design Model (CDM) - a reduced order model used to develop the control law.

2.1 Truth Model

The Truth Model is a nonlinear model using first order physics principles to describe the longitudinal dynamics of a 2D air-breathing hypersonic vehicle. This model captures the interactions between the aerodynamics of the vehicle, propulsion system, and structural dynamics. It expands previous work done in the early 1990s by Chavez and Schmidt[6] focused on the now canceled National Aerospace Plane (NASP). The whole model is coded up in Matlab.

The very basic vehicle geometry used in the model is seen in Figure 2.1. L_v is the vehicle length, which lies along the longitudinally based x-axis, while the z-axis points down. The oblique and bow shock waves are determined by the incoming flow velocity, M_∞, and angle of attack, α.

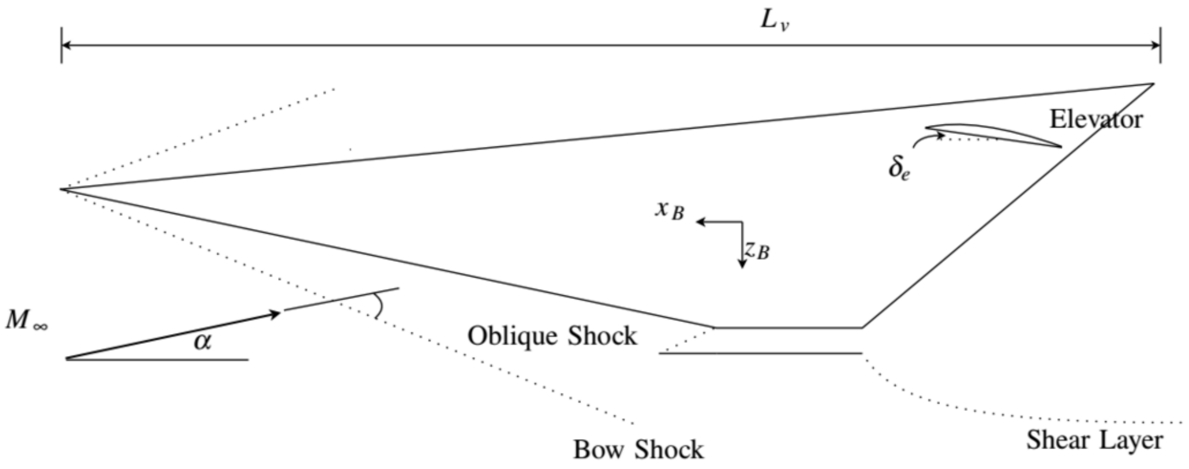

Figure 2.1: Generalized Hypersonic Vehicle Geometry[1]

2.1.1 Aerodynamic Forces

The pressures on the upper and lower forebody are determined by oblique shock and Prandtl-Meyer theory. If the angle between the flow and the surface or ramp it interacts with is greater than 0, an oblique shock occurs. It is assumed that the shock wave is attached at all times. If that angle is less than 0, then a Prandtl-Meyer expansion fan develops.

Pitch control for this hypersonic vehicle is provided by an all-movable elevator. The elevator control surface is modeled as a flat plate. Pressures on the upper and lower surface are calculated using oblique shock and Prandtl-Meyer theory. An option to use a canard as well as an elevator exists, which would undo the pitch-lift coupling that occurs when only an elevator is present.

However, the control law developed explores how to handle a non-minimum phase vehicle. The non-minimum phase behavior is expressed by the physics of the vehicle as follows: When the elevator is deflected down, which increases the pitch rate while at the same time decreasing lift. This causes the flight path angle to temporarily decrease due to the immediate change in lift until the flight path angle increases from the change in angle of attack.

Viscous effects are also modeled.[14] Compressible and turbulent flow is assumed to cover the whole vehicle, for which the skin friction coefficient, c_f, as a function of the Reynold's number is known.[15] The shear stress at the surface is then[14]

$$\tau_w = \frac{1}{2}\rho V^2 c_f \tag{2.1}$$

The total viscous affect can be calculated by integrating the shear stresses over the whole vehicle and then separating the total integrated forces into lift, drag, and pitching moment.

2.1.2 Propulsion

Air-breathing hypersonic vehicles cannot be powered by traditional turbojets or even ramjets. The losses and ram drag caused by slowing down the air to subsonic speeds will be greater than the thrust produced by the engine. Therefore, scramjets (supersonic combusting ramjets) are the only option. Unfortunately, theses scramjets can only be started once they reach a high enough speed (Mach 3 or 4), and the vehicle must be accelerated to those speeds by other means. That phase of propulsion, from subsonic to hypersonic, will not be discussed here, where the focus is on the hypersonic flight phase.

The scramjet is modeled as Rayleigh flow, which is flow through a constant area duct with heat addition. Friction is assumed to be negligible. The engine inlet conditions are determined from the air properties after the bow shock. The bow shock from the leading edge of the vehicle provides the only compression for the air entering the engine. The air entering the engine could be further slowed and compressed in an isentropic diffuser, but for this model the area ratio of the diffuser is fixed at 1, which does not affect the air flow entering the combustor. For this engine model, some more simplifying assumptions are made. The diffuser and nozzle are assumed to be isentropic. In addition, the combustion efficiency is assumed to be 0.9 and the value for c_p, or the specific heat of air at constant pressure, is assumed to be constant, although in reality it will change with temperature.

The scramjet model also takes into account changes in the mass flow through the engine for different Mach numbers and angles of attack. While the ideal case would have the cowl lip of the engine just barely impinge on the bow shock from the nose, called the on design condition, most situations do not fall in this category. For larger angles of attack than the on-design condition, the shock angle is greater, and therefore spillage occurs. However, Bolender and Doman explore this phenomenon and find that even though a larger percentage of the air does not enter the engine, the total capture area increases, so a similar amount of air enters the engine at all conditions. The amount of thrust produced is determined by ϕ, the equivalence ratio, where a value of one is correct stoichiometric ratio. This parameter determines the amount of fuel that enters the combustion chamber and therefore determines the heat release and temperature rise inside the combustion tube. The input ϕ is one of the two control inputs for this model. Upon exiting the combustor, the heated gases enter a diverging nozzle, which is just the lower aftbody of the hypersonic vehicle, and is assumed isentropic.

2.1.3 Unsteady Effects

Unsteady forces are accounted for using first-order hypersonic piston theory. Unsteady aerodynamics are especially important to hypersonic vehicles, because the long slender shapes are flexible enough to make a significant contribution to the aerodynamic forces through structural deformation and vibrations. Unsteady effects are also caused by pitch rates. Piston theory on supersonic airfoils was developed over 60 years ago. The unsteady affects due to rigid body and flexible motion are accounted for in this model.[16]

$$\frac{P}{P_\infty} = \left(1 + \frac{\gamma - 1}{2}\frac{V_n}{a_\infty}\right)^{\frac{2\gamma}{\gamma-1}} \tag{2.2}$$

The first order binomial expansion of this leads to

$$P = P_\infty + \rho_\infty a_\infty V_n \tag{2.3}$$

where V_n is the velocity of the piston perpendicular to the air velocity. The velocity normal to the flow of air is

$$V_n(x,t) = \sum_{i=1}^{3} \dot{\eta}_i(t)\phi_i(x) + Q(t)(x_{c.g.} - x) \tag{2.4}$$

The rigid body unsteady forces and moments due to unsteady effects from the pitch and flexible motions of the aircraft are accounted for.

2.1.4 Structural Dynamics

A flexible model of the hypersonic vehicle is included in the simulation. It is modeled as a free-free beam. Only transverse displacements are considered in this model. For the flexible solution, it was assumed that the displacements were small, so that Hooke's law applied. The second moment of area about the axis of rotation is assumed constant. The modulus of elasticity for the beam material (titanium) is allowed to vary according to different temperatures experienced at different phases of flight. A key feature of hypersonic aerothermoelasticity - the effect of heating on structural stiffness - is, thus, captured.

$$EI\frac{\partial^4\omega(x,t)}{\partial x^4} + \hat{m}\frac{\partial^2\omega(x,t)}{\partial t^2} = 0 \tag{2.5}$$

The solution is assumed to take the form $\omega(x,t) = \phi(x)f(t)$. From this, a set of orthogonal mode shapes, ϕ_k, were found. For the forced time response, there are distributed loads (pressure across vehicle) and concentrated loads (control surface forces).

$$\omega(x,t) = \sum_{k=1}^{\infty} \phi_k(x)\eta_k(t) \tag{2.6}$$

$$N_k(t) = \int_0^L \phi_k(x)p(x,t)dx + \sum_{j=1}^{l} \phi(x_j)P_j(t) \tag{2.7}$$

There are l concentrated loads with force P, and the distributed load is p. In the original model, $p(x,t)$ is the pressure difference across the vehicle due to steady state pressure forces, but excludes unsteady pressures. The nose will be considered $x = 0$ and x is positive at the rear. Only the first three flexible modes are considered in this model.

2.1.5 Equations of Motion

Lagrange's equations were used to derive the equations of motion for the flexible vehicle. The end result is the stability axis equations of motion:[11]

$$\dot{V} = \frac{T\cos\alpha - D}{m} - g\sin\gamma \tag{2.8}$$

$$\dot{h} = V\sin\gamma \tag{2.9}$$

$$\dot{\gamma} = \frac{L + T\sin\alpha}{mV} - \frac{g}{V}\cos\gamma \tag{2.10}$$

$$\dot{\alpha} = -\frac{L + T\sin\alpha}{mV} + Q + \frac{g}{V}\cos\gamma \tag{2.11}$$

$$\dot{Q} = \frac{M}{I_{yy}} \tag{2.12}$$

$$\ddot{\eta}_i = -2\zeta_i\omega_i\dot{\eta}_i - \omega_i^2\eta_i + N_i \tag{2.13}$$

2.1.6 Linear Stability Analysis

The hypersonic vehicle was trimmed at Mach 10 with a dynamic pressure of 1500 psf (near 100,000 ft), and then linearized about this trim condition. The open loop poles are shown in Figure 2.2. The three modes in a diagonal pattern from the origin are the poles for the three aeroelastic modes. The pole in the right half plane represents an unstable short period mode. The zero in the right half plane indicates the non-minimum phase behavior. A deflection of the elevator's trailing edge up will increase angle of attack to increase flight path angle. However, that same elevator deflection also decreases lift, which initially makes the flight path angle decrease.

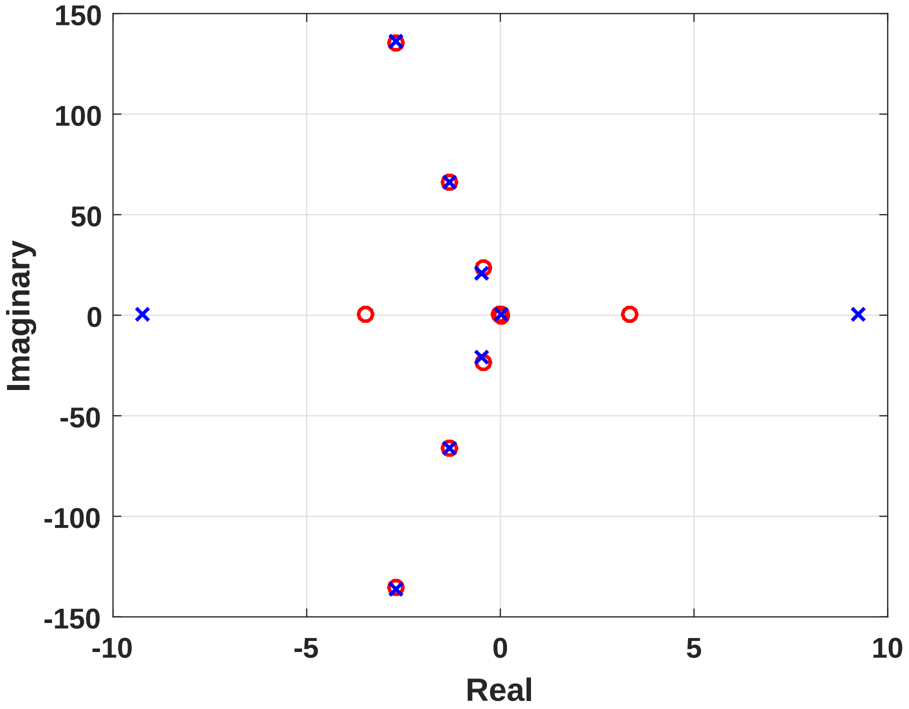

Figure 2.2: Poles and Zeros of Linearized Hypersonic Vehicle Trimmed at M=10 and $\bar{q} =$ 1500psf. Poles (Circles) and Zeros (x's)

Chapter 3

CONTROLLER DESIGN

A control law for a non-minimum phase 2D air-breathing hypersonic vehicle was developed by McKenna and Narang-Siddarth.[2] This control design took advantage of the different time scales of the state variables. A sequential control law was synthesized.

Approaching the control law synthesis task, a Control-oriented Design Model (CDM) of the system had to be developed first because of the complexity of the "high fidelity" math model. Order reduction was necessary to create the controller and analyze its stability. For notation used in this chapter, the reader is referred to Reference[2, 11]

3.1 Control Design Model

The development of the CDM followed the work of Fiorentini *et al.*[11] The forces and moments were curve fitted to base functions of both the rigid body and flexible states. The resulting nonlinear reduced order model still captures the complex dynamical interactions between flexible and rigid dynamic modes as well as the interactions between thrust and elevator inputs. The forces and moments are calculated from their non-dimensional coefficients (expressed as functions of the states and inputs) as well as dynamic pressure:

$$L \approx \frac{1}{2}\rho V^2 S C_L(\alpha, \delta_e, \eta_i) \tag{3.1}$$

$$D \approx \frac{1}{2}\rho V^2 S C_D(\alpha, \delta_e, \eta_i) \tag{3.2}$$

$$T \approx \frac{1}{2}\rho V^2 S C_T(\alpha, \phi, \eta_i) \tag{3.3}$$

$$M_y \approx z_T T(\alpha, \phi, \eta_i, V) + \frac{1}{2}\rho V^2 S \bar{c} C_M(\alpha, \delta_e, \eta_i) \tag{3.4}$$

Note that the pitching moment, in addition to dependency on aerodynamic pressure distributions, is also explicitly a function of thrust, with z_T being the offset between the center of gravity of the vehicle and the location of the scramjet engine on the underside of the vehicle. The coefficients were found by surface fitting them across the entire flight envelope of the hypersonic vehicle:[11]

$$C_L = C_L^{\alpha}\alpha + C_L^{\delta_e}\delta_e + C_L^0 + C_L^{\eta_1}\eta_1 + C_L^{\eta_2}\eta_2 + C_L^{\eta_3}\eta_3 \tag{3.5}$$

$$C_D = C_D^{\alpha^2}\alpha^2 + C_D^{\alpha}\alpha + C_D^{\delta_e^2}\delta_e^2 + C_D^{\delta_e}\delta_e + C_D^0 + C_D^{\eta_1}\eta_1 + C_D^{\eta_2}\eta_2 + C_D^{\eta_3}\eta_3 \tag{3.6}$$

$$C_M = C_M^{\alpha^2}\alpha^2 + C_M^{\alpha}\alpha + C_M^{\delta_e}\delta_e + C_M^0 + C_M^{\eta_1}\eta_1 + C_M^{\eta_2}\eta_2 + C_M^{\eta_3}\eta_3 \tag{3.7}$$

$$C_T = C_T^{\alpha^3\phi}\alpha^3\phi + C_T^{\alpha^2\phi}\alpha^2\phi + C_T^{\alpha\phi}\alpha\phi + C_T^{\phi}\phi + C_T^{\alpha^3}\alpha^3 + C_T^{\alpha^2}\alpha^2 + C_T^{\alpha}\alpha + C_T^0 + \sum_{i=1}^{3} C_T^{\eta_i}\eta_i \tag{3.8}$$

An example curve fit is shown in Figure 3.1. Differences between the surface-fitted math model and the full set of data used to create it cannot be presented in graphic form because of the number of independent variables involved. The x's above and below the surface fit in the figure represent deviations of the fitted model to the data used in a case where graphical presentation is limited to dependency on just two variables.

Simplifying and combining some coefficients, the control design equations of motion are:

$$\dot{M} = c_0(\alpha, M, \eta) + c_1(\alpha, M)\phi\cos\alpha + c_2(M)\delta_e + c_3(M)\delta_e^2 - c_4\sin(\gamma) \tag{3.9}$$

$$\dot{\alpha} = -c_5(\alpha, M, \eta) - \frac{c_1(\alpha, M)}{M}\phi\sin\alpha + c_6(M)\delta_e + Q + \frac{c_4}{M}\cos(\gamma) \tag{3.10}$$

$$- c_7 M\cos(\gamma) \tag{3.11}$$

$$\dot{Q} = c_8(\alpha, M, \eta) + c_9(\alpha, M)\phi + c_{10}(M)\delta_e \tag{3.12}$$

$$\dot{h} = M v_s \sin(\gamma) \tag{3.13}$$

$$\dot{\theta} = Q \tag{3.14}$$

The c_i coefficients are defined in Appendix A.

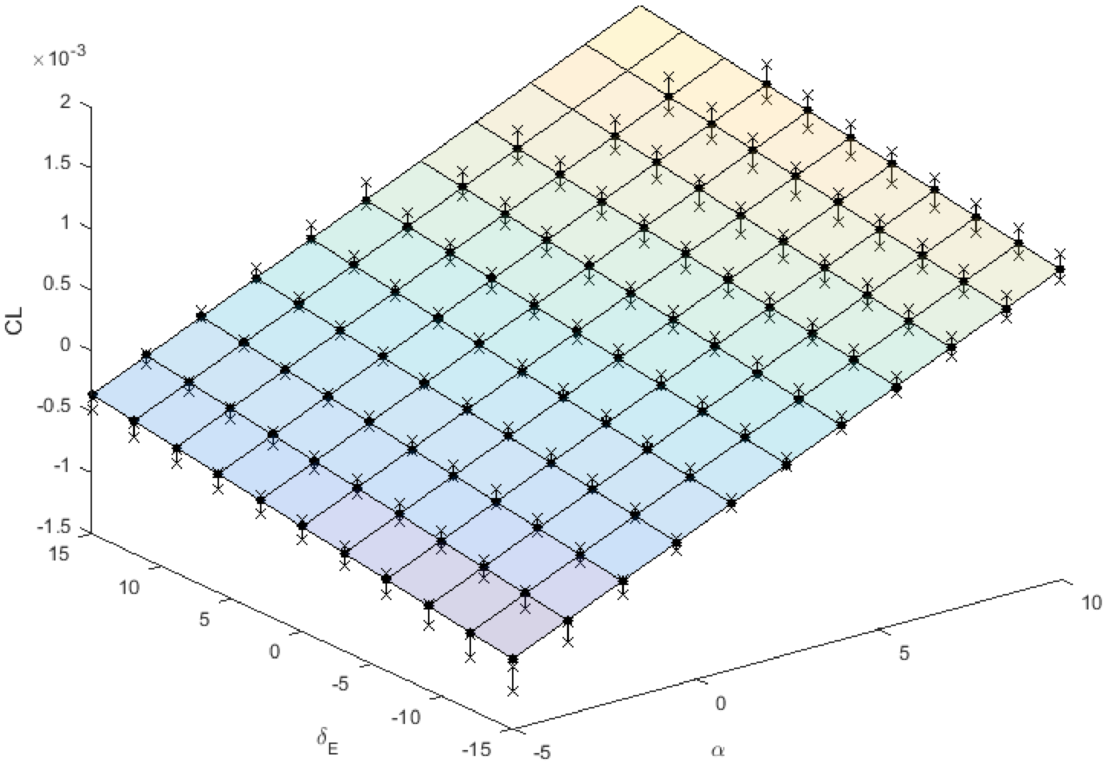

Figure 3.1: C_L Curve-Fit over Hypersonic Vehicle Domain[2]

3.2 Original Controller

An overview of the original controller is shown in Figure 3.2. Flight path angle, γ, and Mach number, M, are the slow states, with angle of attack, α, the moderately fast state, and pitch rate, Q, being the fast state. The equivalence ratio, ϕ is considered a slow actuator, and the elevator command, δ_e, is considered a fast actuator.

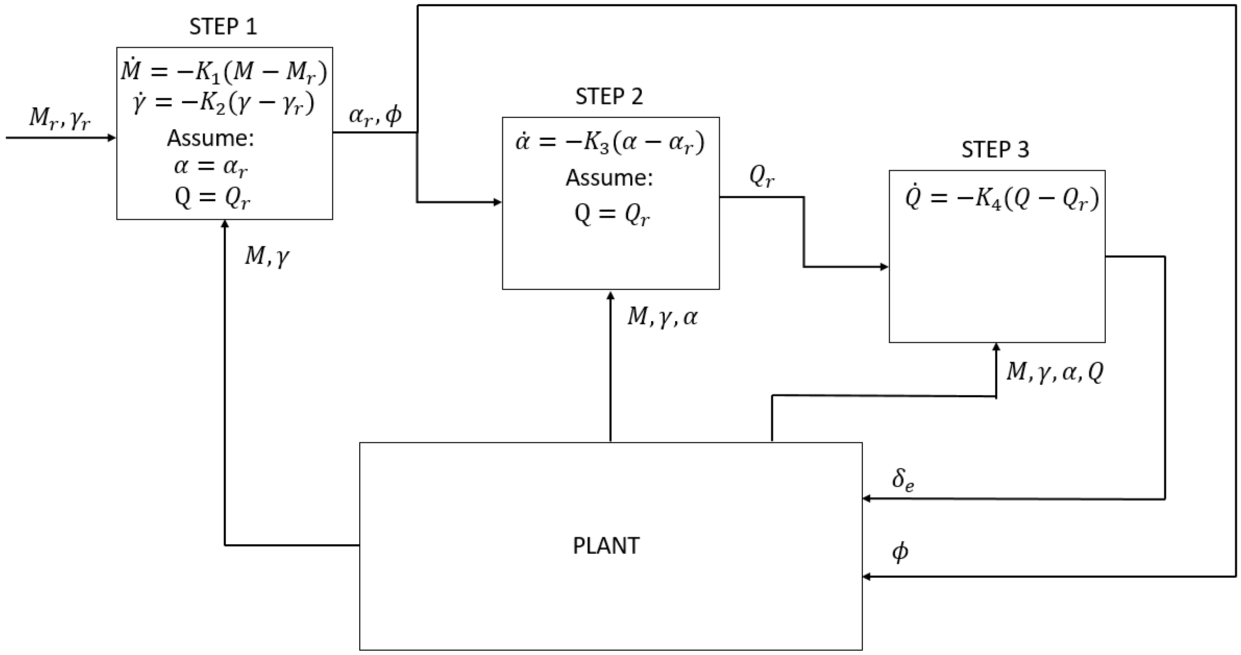

Figure 3.2: Indirect Manifold Approach[2]

To start, it was assumed that the fast states had reached an equilibrium:

$$\alpha = \alpha_r$$

$$Q = Q_r$$

Now the equivalence ration, ϕ_r, and angle of attack, α_r, can be calculated to satisfy the desired rate of change in M and γ for given reference values and gain values K_1 and K_2, and assuming that the pitch rate has settled to its desired value:

$$\dot{M} = -K_1(M - M_r) \tag{3.15}$$

$$\dot{\gamma} = -K_2(\gamma - \gamma_r) \tag{3.16}$$

$$\tag{3.17}$$

Given α_r and ϕ_r, the necessary pitch rate, Q, can be calculated to track the desired rate of change in α given gain value K_3:

$$\dot{\alpha} = -K_3(\alpha - \alpha_r) \tag{3.18}$$

Once the necessary pitch rate, Q_r, is calculated, the elevator deflection that is required to produce that pitch rate can be determined from

$$\dot{Q} = -K_4(Q - Q_r) \tag{3.19}$$

As seen in Figure 3.3, while the Mach number tracking of the original controller is slow but adequate, the flight path angle tracking is very poor. Depending on the relation between actual and desired Mach number, the flight path angle can vary from the desired flight path angle by as much as 0.5 degrees, which translates to very large changes in altitude at such high hypersonic velocities. A few small modifications can be made to this controller to improve the performance.

3.2.1 Step 1

Previous work on this project improperly replaced the functions below with "simpler" functions. The incorrect analysis is shown below in Equations 3.20 and 3.21:

$$c_0(\alpha_r, M) = \frac{\bar{q}S}{mM^2 v_s}(t_0 \cos\alpha_r - d_0) \tag{3.20}$$

The sinusoidal fit and first order polynomial curve fits of the coefficient driver functions are shown below, where s_i and p_i represent the values of the constants used in the curve fits:

$$t_0 \cos\alpha_r - d_0 \approx s_1 \cos\left(\frac{\alpha_r}{s_2}\right) + s_3 \tag{3.21}$$

However, $\left[s_1 \cos\left(\frac{\alpha_r}{s_2}\right) + s_3\right]$ is reduced to $[s_1 + s_3]$ due to the incorrect assumption that $\cos\left(\frac{\alpha_r}{s_2}\right) \approx 1$

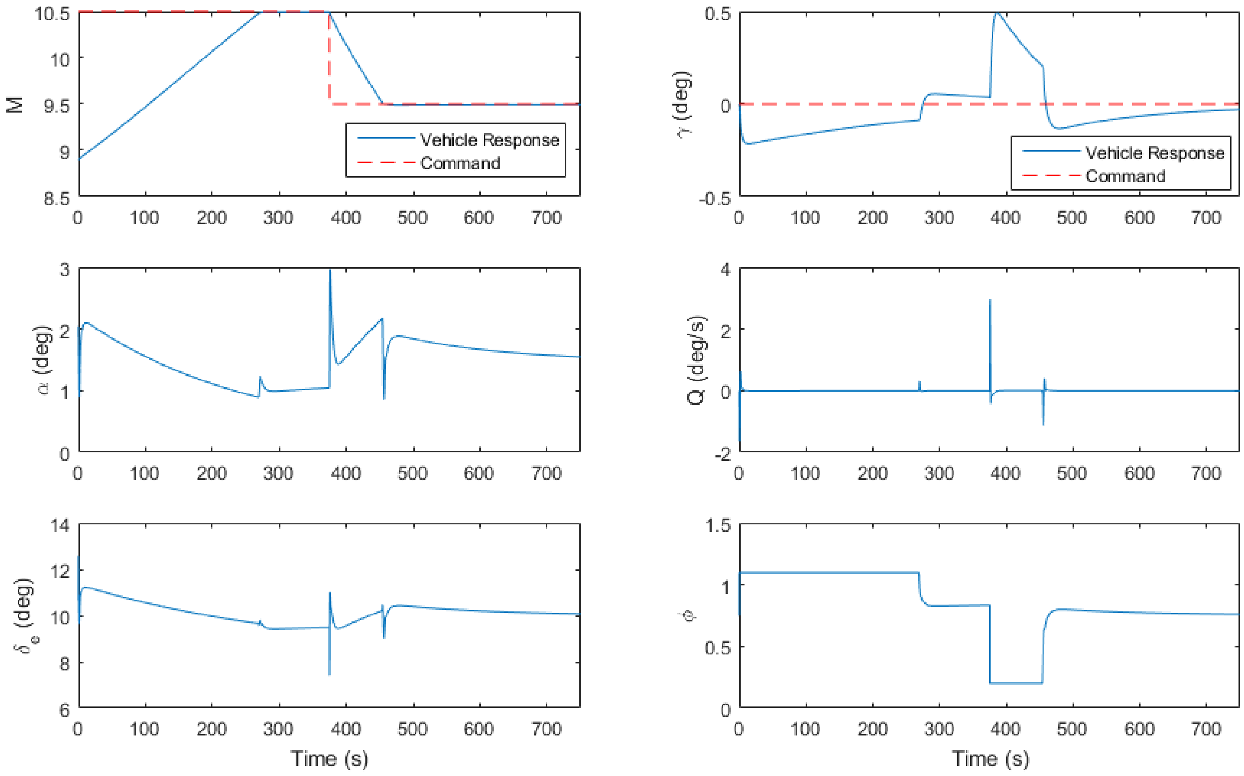

Figure 3.3: Time Simulation of Closed Loop System with Original Control Design[2]

To correct this, we recognize that $c_0(\alpha_r, M) = \frac{\bar{q}S}{mM^2 v_s}(t_0 \cos \alpha_r - d_0)$ is more related to a quadratic function at small angles of attack than a sinusoidal function. Plots of the driver functions below are shown in Reference[2] Also, the previous work neglected the influence of the flexible states, which have a near linear effect on the coefficient driver functions:

$$t_0 \cos \alpha_r - d_0 \approx s_0 + s_1 \eta_1 + s_2 \alpha_r^2 \tag{3.22}$$

$$t_1 \approx p_0 + p_1 \alpha_r \tag{3.23}$$

$$t_0 \sin \alpha_r - l_0 \approx r_0 + r_1 \eta_1 + r_2 \alpha_r \tag{3.24}$$

Reworking the control problem to solve for α_r and ϕ, we now have:

$$\phi = \frac{-K_1(M - M_r) - q^*(s_0 + s_1\eta_1 + s_2\alpha_r^2) - c_2\delta_{e_\zeta} - c_3\delta_{e_\zeta}^2 + c_4\sin(\gamma)}{q^*(p_0 + p_1\alpha_r)} \tag{3.25}$$

$$\sin(\alpha_r) = \frac{M\left[-K_2(\gamma - \gamma_r) - \frac{q^*}{M}(r_0 + r_1\eta + r_2\alpha_r) + c_6\delta_{e_\zeta} + \frac{c_4}{M}\cos(\gamma) - c_7 M\cos(\gamma)\right]}{q^*(p_0 + p_1\alpha_r)\phi} \tag{3.26}$$

Solving for ϕ, we get

$$\phi = \frac{M\left[-K_2(\gamma - \gamma_r) - \frac{q^*}{M}(r_0 + r_1\eta + r_2\alpha_r) + c_6\delta_{e_\zeta} + \frac{c_4}{M}\cos(\gamma) - c_7 M\cos(\gamma)\right]}{q^*(p_0 + p_1\alpha_r)\sin(\alpha_r)} \tag{3.27}$$

Now set the ϕ equations equal to each other and solve for α_r:

$$z_1 = -K_1(M - M_r) - q^*(s_0 + s_1\eta_1) - c_2\delta_{e_\zeta} - c_3\delta_{e_\zeta}^2 + c_4\sin(\gamma) \tag{3.28}$$

$$z_2 = -K_2(\gamma - \gamma_r) - \frac{q^*}{M}(r_0 + r_1\eta) + c_6\delta_{e_\zeta} + \frac{c_4}{M}\cos(\gamma) - c_7 M\cos(\gamma) \tag{3.29}$$

$$z_1 - q^* s_2\alpha_r^2 = \frac{z_2 - q^* r_2\alpha_r}{\sin(\alpha_r)} \tag{3.30}$$

$$-q^* s_2\alpha_r^3 + (z_1 + q^* r_2)\alpha_r - z_2 = 0 \tag{3.31}$$

When working with small angles of attack, $\sin(\alpha_r) \approx \alpha_r$, and therefore $\alpha_r^3 \ll 1$ can be neglected:

$$(z_1 + q^* r_2)\alpha_r - z_2 = 0 \tag{3.32}$$

$$\alpha_r = \frac{z_2}{z_1 + q^* r_2} \tag{3.33}$$

$$\phi = \frac{z_1 - q^* s_2\alpha_r^2}{q^*(p_0 + p_1\alpha_r)} \tag{3.34}$$

Another option is to model the driver function in Equation 3.22 as linear with respect to α_r:

$$t_0\cos\alpha_r - d_0 \approx s_0 + s_1\eta_1 + s_2\alpha_r \tag{3.35}$$

Using the same analysis as before, we get

$$\phi = \frac{-K_1(M - M_r) - q^*(s_0 + s_1\eta_1 + s_2\alpha_r) - c_2\delta_{e_\zeta} - c_3\delta_{e_\zeta}^2 + c_4\sin(\gamma)}{q^*(p_0 + p_1\alpha_r)} \tag{3.36}$$

$$\sin(\alpha_r) = \frac{M\left[-K_2(\gamma - \gamma_r) - \frac{q^*}{M}(r_0 + r_1\eta + r_2\alpha_r) + c_6\delta_{e_\zeta} + \frac{c_4}{M}\cos(\gamma) - c_7 M\cos(\gamma)\right]}{q^*(p_0 + p_1\alpha_r)\phi} \tag{3.37}$$

Solving for ϕ,

$$\phi = \frac{M\left[-K_2(\gamma - \gamma_r) - \frac{q^*}{M}(r_0 + r_1\eta + r_2\alpha_r) + c_6\delta_{e_\zeta} + \frac{c_4}{M}\cos(\gamma) - c_7 M\cos(\gamma)\right]}{q^*(p_0 + p_1\alpha_r)\sin(\alpha_r)} \tag{3.38}$$

The variables z_1 and z_2 have the same formulation as before. Again we make the small angle assumption that $\sin(\alpha_r) \approx \alpha_r$:

$$z_1 - q^* s_2\alpha_r = \frac{z_2 - q^* r_2\alpha_r}{\sin(\alpha_r)} \tag{3.39}$$

$$-q^* s_2\alpha_r^2 + (z_1 + q^* r_2)\alpha_r - z_2 = 0 \tag{3.40}$$

One can solve for α_r with the quadratic formula

$$\alpha_r = \frac{-(z_1 + q^* r_2) + \sqrt{(z_1 + q^* r_2)^2 - 4z_2 q^* s_2}}{-2q^* s_2} \tag{3.41}$$

The addition, rather the subtraction, of the square root term being the answer that makes sense here.

As seen in Figure 3.4, there is minimal difference between the three methods for calculating α_r. The cubic linearized method, because it is the simplest, will be chosen for use in the upcoming stability analysis.

The rest of the control law derivation in the previous work is correct and shown below.

3.2.2 Step 2

The next step outlined[2] in the hierarchical control design is to assume that Q has settled down to some Q_r and that some control input δ_{e_ψ} is being applied. The dynamics of $\dot{\alpha}$ can

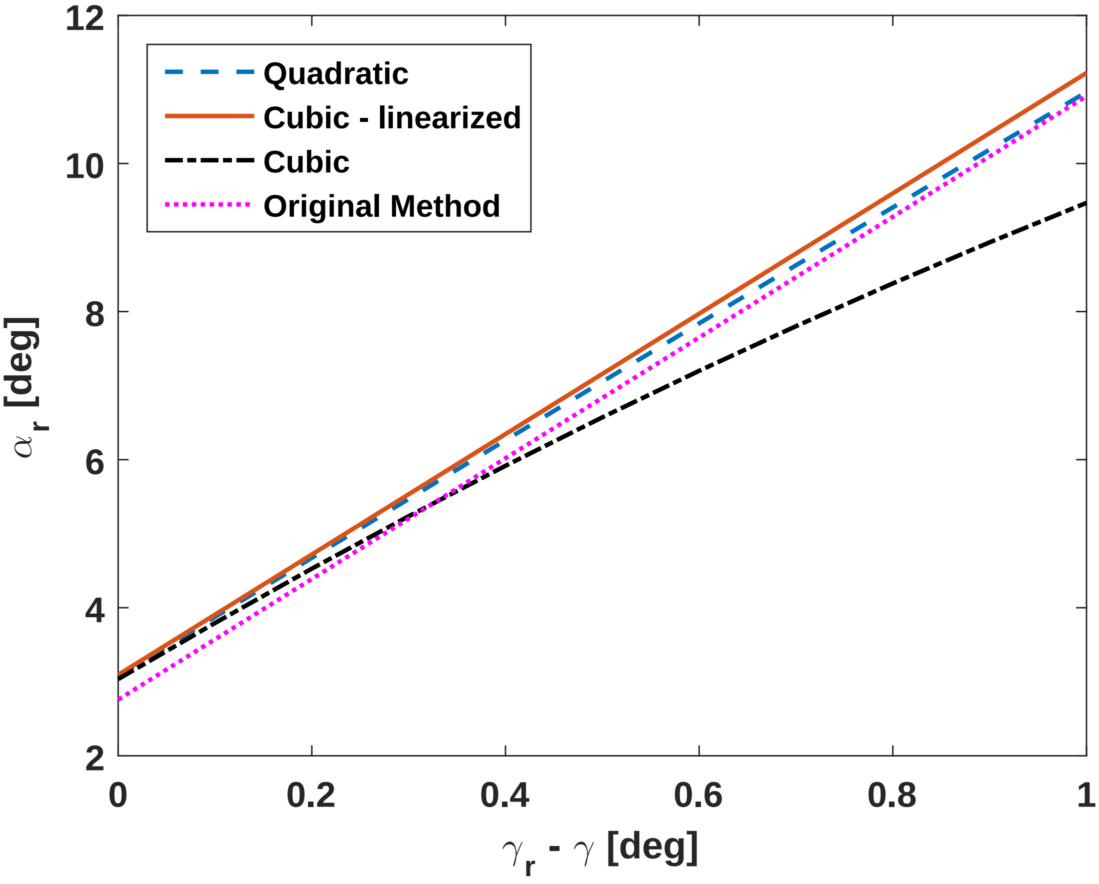

Figure 3.4: Comparison of different methods for calculating α_r

be forced as shown below:

$$\dot{\alpha} = -K_3(\alpha - \alpha_r) \tag{3.42}$$

$$Q_r - \dot{\gamma} = -K_3(\alpha - \alpha_r) \tag{3.43}$$

Substituting the $\dot{\gamma}$ equation of motion gives the complete equation needed to solve for Q_r:

$$Q_r - c_5(\alpha) - \frac{c_1(\alpha, M)}{M}\phi \sin\alpha + c_6(M)\delta_{e_\psi} + \frac{c_4}{M}\cos(\gamma) - c_7 M \cos(\gamma) = -K_3(\alpha - \alpha_r) \tag{3.44}$$

The equation for Q_r is now obtained:

$$Q_r = c_5(\alpha) + \frac{c_1(\alpha, M)}{M}\phi \sin\alpha - c_6(M)\delta_{e_\psi} - \frac{c_4}{M}\cos(\gamma) + c_7 M \cos(\gamma) - K_3(\alpha - \alpha_r) \quad (3.45)$$

3.2.3 Step 3

The final step outlined[2] in the control design is forcing the dynamics of the second internal state, $\dot{Q}$:

$$\dot{Q} = -K_4(Q - Q_r) \quad (3.46)$$

The following equation is taken from the original equations of motion:

$$\dot{Q} = c_8(\alpha, M) + c_9(\alpha, M)\phi + c_{10}(M)\delta_e = -K_4(Q - Q_r) \quad (3.47)$$

A solution for the δ_e required to force the dynamics in the proper manner can now be explicitly stated:

$$\delta_e = \frac{1}{c_{10}(M)}\left[-K_4(Q - Q_r) - c_8(\alpha, M) - c_9(\alpha, M)\phi\right] \quad (3.48)$$

Along with the equation for δ_e, the interim control inputs δ_{e_ζ} and δ_{e_ψ} can also be solved for. The resulting solutions are shown below:

$$\delta_{e_\zeta} = \frac{1}{c_{10}(M)}\left[-c_8(\alpha_r, M) - c_9(\alpha_r, M)\phi\right] \quad (3.49)$$

$$\delta_{e_\psi} = \frac{1}{c_{10}(M)}\left[-c_8(\alpha, M) - c_9(\alpha, M)\phi\right] \quad (3.50)$$

The controller tracks to the desired outputs, but does include some error between the desired and steady state Mach number and flight path angle.

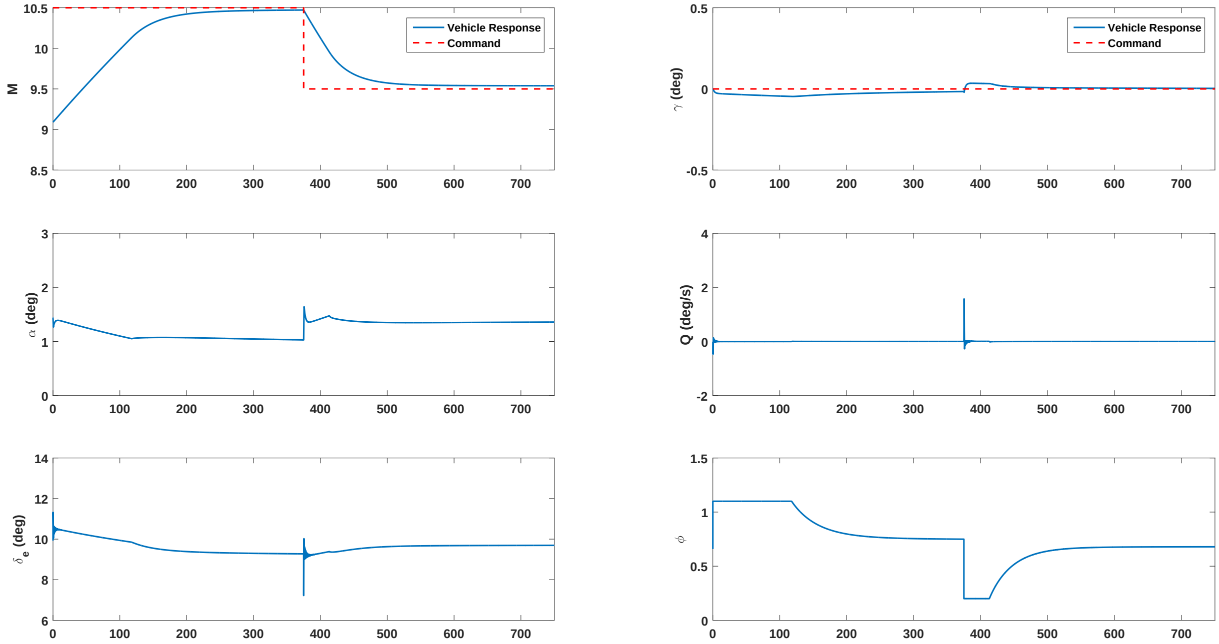

Figure 3.5: Time Simulation of Closed Loop System with Fixed Original Controller

3.3 New Controller

An adaptive nonlinear hierarchical control law was developed by Fiorentini[11] for a hypersonic vehicle with a canard and elevator. This new control law synthesized here takes her approach but leaves out the canard used to get rid of the non-minimum phase behavior. Unfortunately, possibly due to the non-minimum phase behavior, the adaptive part was unable to be implemented successfully. The following control law does not make any assumptions that separate states into slow and fast time scales. An overview of the control law is shown in Figure 3.6.

In the original control law, there is slight error between desired and actual Mach number

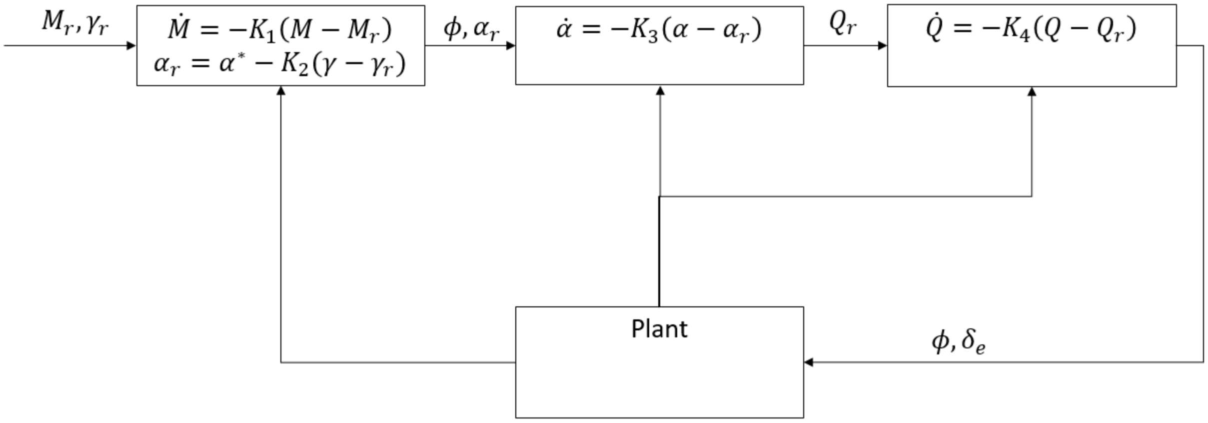

Figure 3.6: Modified Fiorentini Approach

achieved. This is due to the approximations that were made to calculate α_r. However, the derivative of $\dot{M}$ is linear with respect to ϕ. Therefore, we can solve for ϕ directly without assuming that the plant has reached some desired α_r:

$$\dot{M} = c_0(\alpha, M) + c_1(\alpha, M)\phi\cos\alpha + c_2(M)\delta_e + c_3(M)\delta_e^2 - c_4\sin(\gamma) \tag{3.51}$$

$$\dot{M} = -K_1(M - M_r) \tag{3.52}$$

$$\phi = \frac{-K_1(M - M_r) - c_0(\alpha, M) - c_2(M)\delta_e - c_3(M)\delta_e^2 + c_4\sin(\gamma)}{c_1(\alpha, M)\cos(\alpha)} \tag{3.53}$$

This will maintain the full fidelity of the CDM, without making any simplifying assumptions regarding the coefficients that are to the second and third order of angle of attack.

To better maintain the fidelity of the CDM when determining what α_r should be, a similar approach is taken:

$$\dot{\gamma} = c_5(\alpha_r) + \frac{c_1(\alpha_r, M)}{M}\phi\sin(\alpha_r) - c_6(M)\delta_e - \frac{c_4}{M}\cos(\gamma) + c_7 M\cos(\gamma) \tag{3.54}$$

Instead of solving for the exact α_r that will ensure $\dot{\gamma} = -K_2(\gamma - \gamma_r)$, we first determine what the vehicle state will be at the final desired condition. Call this vehicle state $X^* = [M^*, \alpha^*, Q^*, h^*, \theta^*, \eta_n^*]^T$. Therefore, let

$$\alpha_r = \alpha^* - K_2(\gamma - \gamma_r) \tag{3.55}$$

Of course, this requires prior computation of α^* and does not ensure that $\dot{\gamma} = -K_2(\gamma - \gamma_r)$, but the important thing is that α_r will increase or decrease appropriately in proportion to $(\gamma - \gamma_r)$. A benefit of this method is that α_r is not explicitly dependent on the K_1 gain that controls the velocity dynamics.

Q_r and δ_e are now solved for in the same way that they were in the original control design:

$$Q_r = c_5(\alpha) + \frac{c_1(\alpha, M)}{M}\phi \sin\alpha - c_6(M)\delta_{e_\psi} - \frac{c_4}{M}\cos(\gamma) + c_7 M\cos(\gamma) - K_3(\alpha - \alpha_r) \tag{3.56}$$

$$\delta_e = \frac{1}{c_{10}(M)}\left[-K_4(Q - Q_r) - c_8(\alpha, M) - c_9(\alpha, M)\phi\right] \tag{3.57}$$

Figure 3.7 shows that the control law works in simulations and has less steady state error between desired and actual Mach number and flight path angle than the original controller.

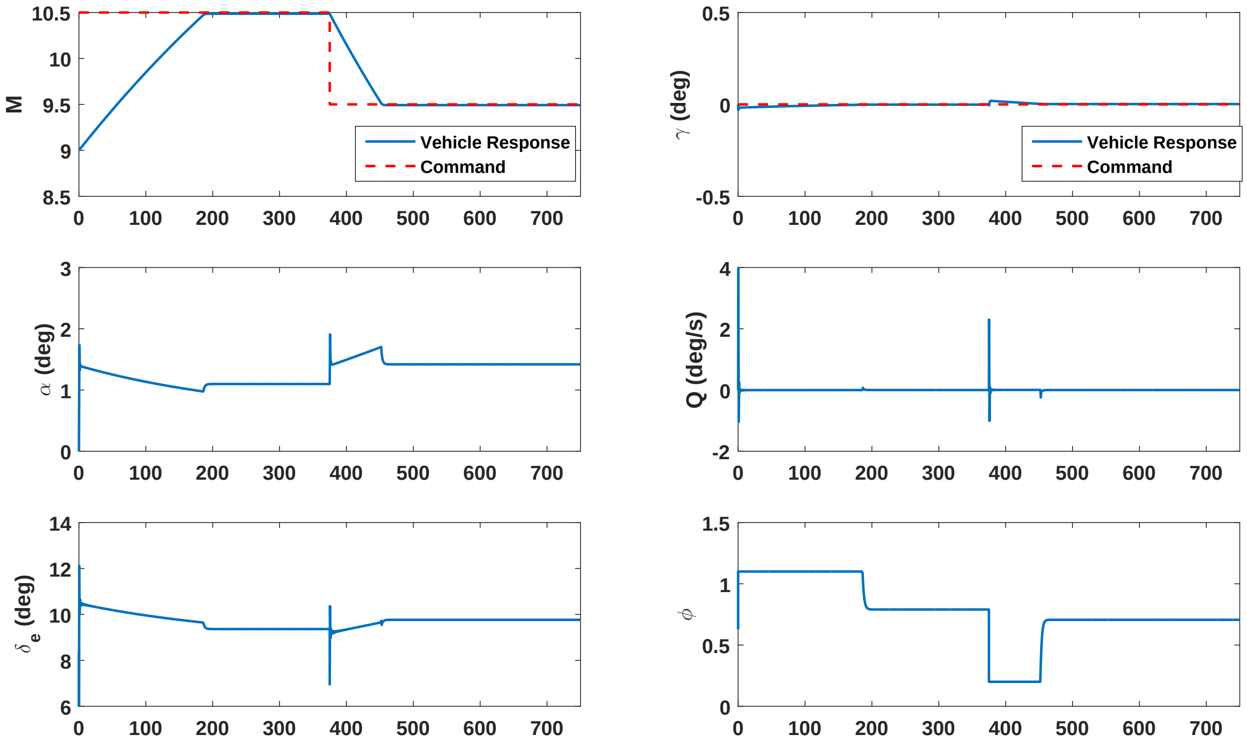

Figure 3.7: Time Simulation of Closed Loop System with New Control Design

Chapter 4

STABILITY ANALYSIS AND GAIN SELECTION

4.1 Lyapunov Stability

The following Lyapunov function for the controlled system is defined as:

$$V = \frac{1}{2}(M - M_r)^2 + \frac{1}{2}(\gamma - \gamma_r)^2 + \frac{1}{2}(\alpha - \alpha_r)^2 + \frac{1}{2}(Q - Q_r)^2 \tag{4.1}$$

This function is positive definite. The derivative of this Lyapunov Function is shown below:

$$\dot{V} = (M - M_r)\dot{M} + (\gamma - \gamma_r)\dot{\gamma} + (\alpha - \alpha_r)(\dot{\alpha} - \dot{\alpha_r}) + (Q - Q_r)(\dot{Q} - \dot{Q}_r) \tag{4.2}$$

Remember that γ_r and M_r are the reference values the system is trying to reach, and while they may be changing in time, for our analysis here they are treated as constant values. The system is considered stable if for all conditions $\dot{V}$ is negative definite.

The previous thesis on this subject attempted to individually bound all derivatives, but incorrectly applied the Lipschitz condition on some terms.[2]

This work finds, but not proves, acceptable gain values using Monte Carlo simulations.

4.1.1 Original Controller Analysis

First, the derivative of the Lyapunov function must be created:

$$\dot{M} = c_0(\alpha, M) + c_1(\alpha, M)\phi\cos\alpha + c_2(M)\delta_e + c_3(M)\delta_e^2 - c_4\sin(\gamma) \tag{4.3}$$

$$\dot{\gamma} = c_5(\alpha) + \frac{c_1(\alpha, M)}{M}\phi\sin(\alpha) - c_6(M)\delta_e - \frac{c_4}{M}\cos(\gamma) + c_7 M\cos(\gamma) \tag{4.4}$$

$$\dot{\alpha} = Q - c_5(\alpha) - \frac{c_1(\alpha, M)}{M} phi \sin(\alpha) + c_6 + \frac{c_4}{M}\cos(\gamma) - c_7 M \cos(\gamma) \tag{4.5}$$

$$\dot{Q} = c_8(\alpha, M) + c_9(\alpha, M) + c_{10}(M)\delta_e \tag{4.6}$$

The derivative of α_r is more complex. Recall that

$$\alpha_r = \frac{z_2}{z_1 + q^* r_2} \tag{4.7}$$

$$q^* = \frac{\bar{q}S}{mV_s} \tag{4.8}$$

$$z_1 = -K_1(M - M_r) - q^*(s_0 + s_1\eta_1) - c_2\delta_{e_\zeta} - c_3\delta_{e_\zeta}^2 + c_4\sin(\gamma) \tag{4.9}$$

$$z_2 = -MK_2(\gamma - \gamma_r) - q^*(r_0 + r_1\eta_1) + Mc_6\delta_{e_\zeta} + c_4\cos(\gamma) - M^2 c_7\cos(\gamma) \tag{4.10}$$

$$\dot{\alpha}_r = \frac{\partial \alpha_r}{\partial M}\dot{M} + \frac{\partial \alpha_r}{\partial \gamma}\dot{\gamma} \tag{4.11}$$

$$\begin{aligned}\frac{\partial \alpha_r}{\partial M} = &\frac{(-K_2(\gamma - \gamma_r) - \frac{\rho M V_s S}{m}(r_0 + r_1\eta_1) + c_6\delta_{e_\zeta} - 2Mc_7\cos(\gamma))(q^* r_2 + z_1)}{(q^* r_2 + z_1)^2} \\ &- \frac{(-K_1 - \frac{\rho M V_s S}{m}(s_0 + s_1\eta_1) - \frac{\rho M V_s S d_1}{m}\delta_{e_\zeta} - \frac{\rho M V_s S d_2}{m}\delta_{e_\zeta}^2)z_2}{(q^* r_2 + z_1 - q^* s_2)^2}\end{aligned} \tag{4.12}$$

$$\frac{\partial \alpha_r}{\partial \gamma} = \frac{(-MK_2 - c_4\sin(\gamma) + M^2 c_7\sin(\gamma))(q^* r_2 + z_1 - q^* s_2) - c_4\cos(\gamma)z_2}{(q^* r_2 + z_1)^2} \tag{4.13}$$

Finally, the derivative of Q_r is found. Recall that,

$$Q_r = c_5(M, \alpha) + \frac{c_1(M, \alpha)}{M}\phi\sin(\alpha) - c_6(M)\delta_{e_\psi} - \frac{c_4}{M}\cos(\gamma) + c_7 M\cos(\gamma) - K_3(\alpha - \alpha_r) \tag{4.14}$$

$$\dot{Q}_r = \frac{\partial Q_r}{\partial M}\dot{M} + \frac{\partial Q_r}{\partial \gamma}\dot{\gamma} + \frac{\partial Q_r}{\partial \alpha}\dot{\alpha} + \frac{\partial Q_r}{\partial \alpha_r}\dot{\alpha}_r \tag{4.15}$$

$$\frac{\partial Q_r}{\partial M} = \frac{\rho V_s S}{2m}(t_0 \sin(\alpha) - l_0 + t_1 \phi \sin(\alpha) - l_1 \delta_{e_\psi}) + (\frac{c_4}{M^2} + c_7)\cos(\gamma) \tag{4.16}$$

$$\frac{\partial Q_r}{\partial \gamma} = (\frac{c_4}{M} - c_7 M)\sin(\gamma) \tag{4.17}$$

$$\frac{\partial Q_r}{\partial \alpha} = \frac{\rho M V_s S}{2m} t_0 \cos(\alpha) + \frac{c_1}{M}\phi\cos(\alpha) - K_3 \tag{4.18}$$

$$\frac{\partial Q_r}{\partial \alpha_r} = K_3 \tag{4.19}$$

Now equations for all the derivatives required to calculate $\dot{V}$ have been created. This function is too complex for analytically proving negative definiteness, and so Monte Carlo methods are used to find a set of suitable gain values that ensure $\dot{V}$ is negative definite for all conditions. The range of conditions that were tested is presented in Table 4.1.

Variable	min	max
M	9	11
Q	0 deg/s	10 deg/s
α	0 deg	10 deg
γ	-3 deg	3 deg

Table 4.1: Range of Flight Conditions Tested

4.2 Max K_1 and K_2 Gains for Original Controller

The control design model (CDM) is valid for 0 deg $\leq \alpha \leq$ 10 deg. We want to ensure we select gains that do not attempt to exceed this boundary. Bringing z_1 and z_2 into the equation for α_r, we get:

$$\alpha_r = \frac{-MK_2(\gamma - \gamma_r) - q^*(r_0 + r_1\eta_1) + Mc_6\delta_{e_\zeta} + c_4\cos(\gamma) - M^2c_7\cos(\gamma)}{-K_1(M - M_r) - q^*(s_0 + s_1\eta_1) - c_2\delta_{e_\zeta} - c_3\delta_{e_\zeta}^2 + c_4\sin(\gamma) + q^*r_2 - q^*s_2} \tag{4.20}$$

We want to single out the K_2 gain:

$$\begin{aligned}\alpha_r\Big(-K_1(M - M_r) - q^*(s_0 + s_1\eta_1) - c_2\delta_{e_\zeta} - c_3\delta_{e_\zeta}^2 + c_4\sin(\gamma) + q^*r_2 - q^*s_2\Big)&\\ = -MK_2(\gamma - \gamma_r) - q^*(r_0 + r_1\eta_1) + Mc_6\delta_{e_\zeta} + c_4\cos(\gamma) - M^2c_7\cos(\gamma)&\end{aligned} \tag{4.21}$$

$$\begin{aligned}-MK_2(\gamma-\gamma_r) = \alpha_r\Big(-K_1(M - M_r) - q^*(s_0 + s_1\eta_1) - c_2\delta_{e_\zeta} - c_3\delta_{e_\zeta}^2 + c_4\sin(\gamma) + q^*r_2 - q^*s_2\Big)&\\ + q^*(r_0 + r_1\eta_1) - Mc_6\delta_{e_\zeta} - c_4\cos(\gamma) + M^2c_7\cos(\gamma)&\end{aligned} \tag{4.22}$$

$$\begin{aligned}K_2 \le \frac{0.175\text{rad}\Big(-K_1(M - M_r) - q^*(s_0 + s_1\eta_1) - c_2\delta_{e_\zeta} - c_3\delta_{e_\zeta}^2 + c_4\sin(\gamma) + q^*r_2 - q^*s_2\Big)}{-M(\gamma - \gamma_r)}&\\ + \frac{q^*(r_0 + r_1\eta_1) - Mc_6\delta_{e_\zeta} - c_4\cos(\gamma) + M^2c_7\cos(\gamma)}{-M(\gamma - \gamma_r)}&\end{aligned} \tag{4.23}$$

For this analysis, assume that $M = M_r$ to single out the K_2 gain. To find the max possible K_2 gain without having $\alpha_r \ge 10$ deg, set $\alpha_r = 10^\circ$ and solve for K_2. Set η_1 to a normal value occurring at $\alpha = 0$ deg. Vary $\Delta\gamma$ and δ_{e_ζ} over their expected range, which for the Monte Carlo analysis is $[0, 1]$deg and $[0, 20]$deg, respectively.

In order to avoid $\alpha_r \ge 10$ deg, the smallest K_2 which occurs when $\Delta\gamma = 1$ deg and $\delta_{e_\zeta} = 0$ deg should be chosen as the max.

A similar analysis can be done with K_1 to avoid breaking the ϕ boundaries of $0.1 \le \phi \le 1.1$.

4.3 Monte Carlo Gain Selection

Gains are to be chosen that minimize $\dot{V}$ over the range of conditions as specified in Table 4.1. Gains K_1 through K_4 will be randomly selected between the following ranges:

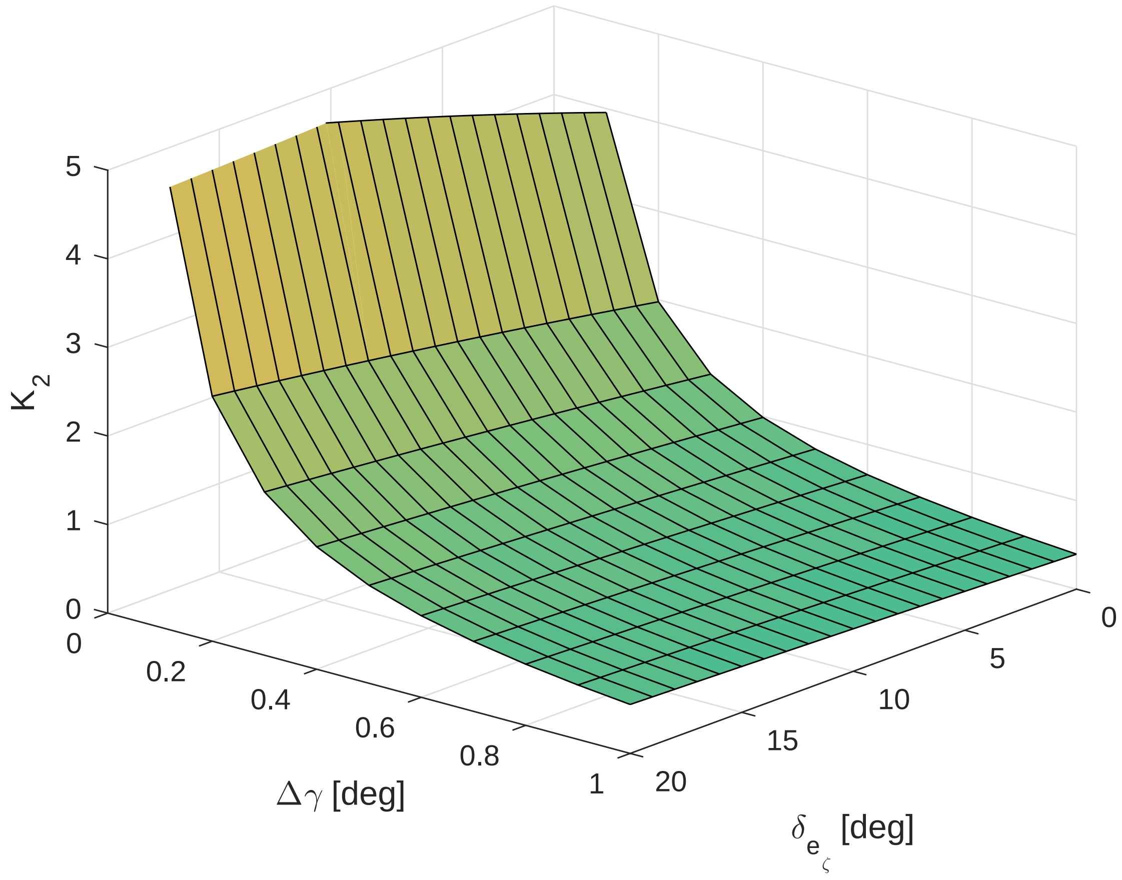

Figure 4.1: Max K_2

For each set of conditions, $\dot{V}$ must remain negative, or the selected gains do not ensure stability. The average of $\dot{V}$ for each set of gains that ensure the negative definiteness will be calculated, and the set of gains with the most negative average $\dot{V}$ will be selected as the optimal gains. At the same time, we do not want to find a set of gains that will violate the control constraints of $-20° \leq \delta_e \leq 20°$. Without factoring this in, it is possible to find a set of gains that will make the controller jump from constraint to constraint, as seen in Figure 4.2, which is undesirable behavior.

Gain	min	max
K_1	0	0.05
K_2	0	0.5
K_3	0	4
K_4	0	10

Table 4.2: Gain Ranges

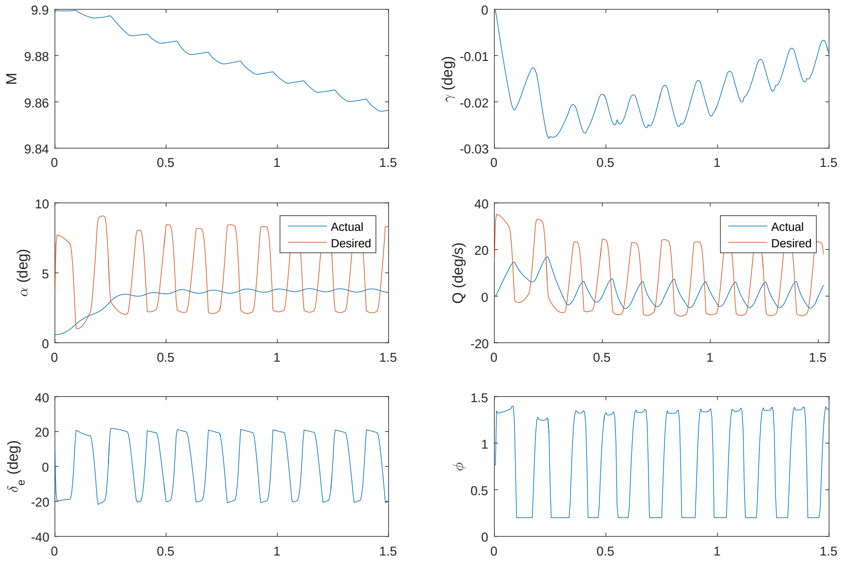

Figure 4.2: The elevator input, δ_e, bounces back and forth between its limits. Gains: $K_1 = 0.05$, $K_2 = 0.48$, $K_3 = 4.95$, $K_4 = 9.95$

The results are plotted in Figure 4.3. The y-axis is the average $\dot{V}$ over the range of flight conditions that were tested. The flight conditions adjusted were α, Q, γ, and γ_r; they were swept across a reasonable range, shown in table 4.1. The K_3 gain is capped at 4

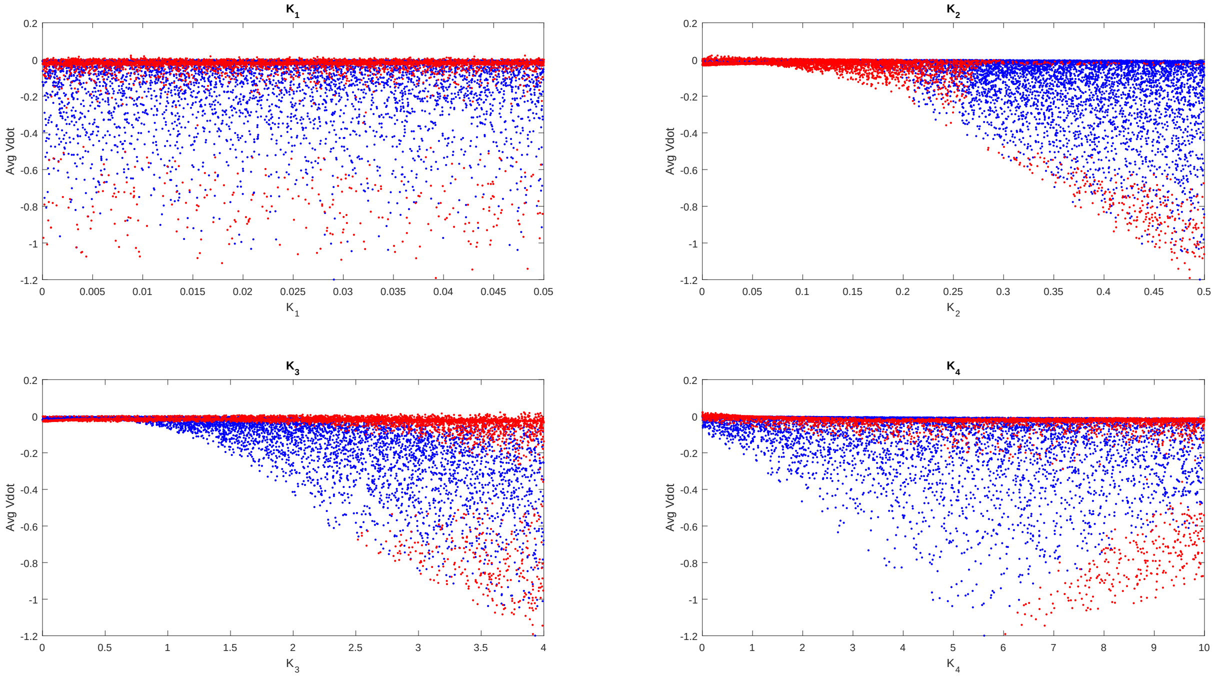

Figure 4.3: How $\dot{V}$ Changes With Each Random Set of Gains (Blue Dots Maintain Negative Definiteness, Red Dots Do Not)

because values beyond that were found to excite the flexible modes. The chosen gains that minimized $\dot{V}$ are in Table 4.3. The nominal trajectory with the chosen optimized gains is shown in Figure 4.4. Notice how, unlike the trajectory in Figure 4.2, the controls stay within their boundaries and the internal dynamics of α and Q is much more smooth.

Gain	Optimal Value
K_1	0.025
K_2	0.46
K_3	3.8
K_4	5.31

Table 4.3: Selected Gains

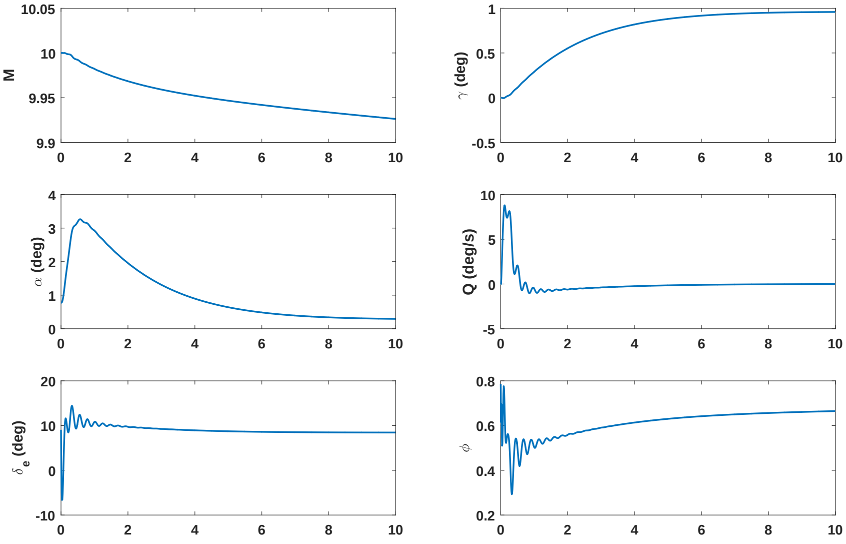

Figure 4.4: Nominal Trajectory With Optimal Gains

Chapter 5

MONTE CARLO ANALYSIS

5.1 Monte Carlo Methods

Monte Carlo methods are used to study probabilistic problems numerically by using large numbers of computer simulations driven by random sampling of the parameters controlling the problems. In general, the input parameters for the simulations are the uncertain parameters. Each simulation generates a new random value of each uncertain parameter based on that parameter's specific statistical distribution. For each simulation, there is a set of outputs. Statistical analysis of the distributions of such outputs sheds light on the way uncertainties propagate and the way the system behaves subject to uncertainty. A flow chart of Monte Carlo methods is presented in Figure 5.1.

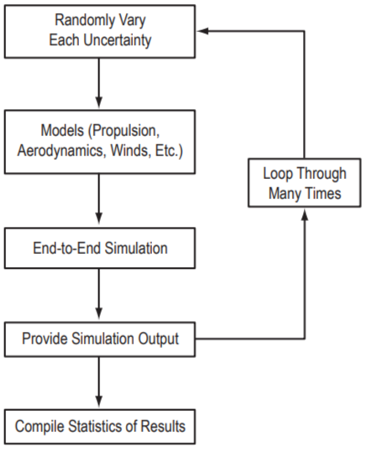

Figure 5.1: Monte Carlo Method[3]

5.1.1 Input Distributions

The majority of the input parameters are given normal probability distributions. Normal distributions are defined by two parameters: the mean (μ) and standard deviation (σ). The probability distribution, p, is given by

$$p_n(x) = \frac{1}{\sqrt{2\pi\sigma^2}} e^{-\frac{(x-\mu)^2}{2\sigma^2}} \tag{5.1}$$

Roughly 68% of the results lie within one standard deviation from the mean and 95% within two standard deviations. For random variables generated from a normal distribution, the random variables will have a probability density function that resembles a normal distribution as the number of random variables, $n \to \infty$.

The other distribution used is the uniform distribution. Over a given interval, the probability distribution is constant. The uniform probability distribution over an interval $[a, b]$ is

$$p_u(x) = \frac{1}{b-a} \tag{5.2}$$

5.1.2 Statistical Analysis

Confidence Interval

Confidence intervals are used to determine how much much confidence there that the true value of a population mean lies within a specified interval, given information about a sample that is normally distributed. A confidence interval is defined as

$$CI = \bar{x} \pm t_{\alpha,n} \frac{s}{\sqrt{N}} \tag{5.3}$$

where $t_{\alpha,n}$ is the Student-T value given a specified accuracy, α, and degrees of freedom, n. The degrees of freedom is the number of samples. For this thesis, a two-tailed 95% confidence interval is used, making $\alpha = \frac{1}{2}(1 - 0.95)$. Note that α here is not the angle of attack designated by α in the previous sections, but rather, the specified accuracy that is designated by α in standard statistical texts.

Linear Regression

In order to find out the effects of each uncertainty on the final flight path angle, linear regression is used to find out the relative contribution of each uncertain variable. The model for the linear regression used is:

$$\gamma_{final} = \beta_0 + \sum_{i=1}^{m} \beta_i p_i \tag{5.4}$$

where p_i is the uncertainty value of the i^{th} parameter and β_i is the slope associated with that parameter, which is obtained from the linear regression:

$$A^{n\times m}\beta^{m\times 1} = y^{n\times 1} \tag{5.5}$$

$$\hat{\beta} = (A^T A)^{-1} A^T y \tag{5.6}$$

Where A is a matrix where each row contains all uncertainty values of a certain parameter, and y is a column vector of outputs. The estimated sensitivity of the uncertain parameter is represented by $\hat{\beta}$, which is a column vector.

Confidence Interval on Regression Coefficients

Confidence interval of the individual regression coefficients ($\hat{\beta}_i$) is defined as follows:

$$\hat{\beta} \pm t_{\alpha,n-(k+1)}\sqrt{C_{jj}} \tag{5.7}$$

where C is the covariance matrix, $t_{\alpha,n-(k+1)}$ is the student-t value with a confidence level $(1-\alpha)\%$, n is the number of observations, and k is the number of predictor variables of the regression, in this case the number of uncertain parameters. As the number of degrees of freedom increases, the student-t value decreases until converging with its relative value for a normal distribution.

To find the standard error (SE) of the individual regression coefficient ($\sqrt{C_{jj}}$), a variety of parameters must be calculated first:

$$C = \hat{\sigma}^2 (A^T A)^{-1} \tag{5.8}$$

where

$$\hat{\sigma}^2 = \text{Mean Squared Error (MSE)}$$

and

$$\text{MSE} = \frac{y^T (I - H) y}{n - (k + 1)} \tag{5.9}$$

$$H = A(A^T A)^{-1} A^T \tag{5.10}$$

If the confidence interval contains 0, then that uncertain parameter does not have a statistically significant effect on the outcome. However, if the confidence interval stays all positive or negative, then that value does have a statistically significant effect on the outcome.

5.2 Model Uncertainty

Accurate modeling of the hypersonic vehicle is a major challenge. At extremely high velocities, aerodynamic heating, shockwave - boundary layer interactions, and changes in air characteristics, are no longer negligible. The geometries involves are complex. Even with more advanced math modeling techniques there will always be sources of modeling uncertainty.

There are two models that are important in this work. The first is what will be called earlier the Truth Model - a high fidelity simulation developed by Michael Bolender and David Doman from the Air Force Research Laboratory at Wright Patterson Air Force Base. The second is the Control Design Model (CDM) - a reduced order model used to develop the control law.

5.2.1 Sources of Uncertainty

There are two classes of uncertainty: (1)epistemic and (2)aleatory. Epistemic uncertainty is uncertainty inherent to the modeling assumptions. Engineers do their best to make the mathematical model capture as much of the real-world behavior of the system as possible, but due to limitations in knowing how the world works (physics), or assumptions explicitly made to make the model easier to work with, the mathematical model will never perfectly represent the physical system. Aleatory uncertainty is uncertainty inherent to input parameters. This could be uncertainty about the atmosphere (it's never actually the standard atmosphere from the tables), or material properties (different manufacturing processes, microscopic cracks), or other inherently random variation in physical systems. Epistemic uncertainty can be reduced through more thorough understanding of the physics of the system or more complex mathematical models. Aleatory uncertainty, while it can be reduced, it cannot be eliminated. The simulations in this work will include both epistemic and aleatory uncertainty.

5.2.2 Atmospheric Uncertainty

This model uses atmospheric data based on the 1976 Standard Atmosphere. Variations from this standard atmosphere, as well as imperfect temperature or pressure sensors are all sources of uncertainty. High velocity hypersonic flows will also create more uncertainty in the ratio of specific heats (γ). It has a well-known value of 1.4 at low speeds. However, as the Mach number increases and likewise the temperature behind the shock, the gas begins to dissociate and the specific heat ratio is no longer a constant.[17]

5.2.3 Propulsion Uncertainty

There are many uncertain input parameters that are used to calculate the thrust generated from the scramjet engine. The calculation of the total temperature of the gas at the combustor exit is given by:

$$\frac{T_{t3}}{T_{t2}} = \frac{1 + H_f \eta_c f_{st} \phi / (c_p T_{t2})}{1 + f_{st} \phi} \tag{5.11}$$

There are three primary parameters in this equation that are uncertain. The heating value of hydrogen (H_f) is based on the lower heating value in the model. However, this is a conservative estimate, because there is also a higher heating value of hydrogen that is roughly 15% higher.[18] The two values are based on how much energy is released when H_2 is combusted at 25 C and returned to 150 C vs 25 C. To stay closer to the conservative estimate, the heating value will vary uniformly between 100% and 105% of the lower heating value. The second parameter in this equation is η_c, the combustion efficiency. Based on unmodeled parameters such as types of fuel injectors and combustion chamber length, the combustion efficiency can vary from 70%-95%.[19] The final uncertain parameter in this equation is c_p, the specific heat of air at a constant pressure. For low speed analysis, c_p is considered constant. However, just as with the ratio of specific heats, c_p begins to vary at high temperatures caused by the vehicle's hypersonic velocities.

The nozzle efficiency is the ratio between the actual exit Mach number at the end of the nozzle, M_e, and the exit Mach number if the nozzle is isentropic:

$$\eta_n = \frac{M_e}{M_{isentropic}} \tag{5.12}$$

The final uncertain parameter affecting the propulsion system is the mass flow into the engine. While this model captures the effect of off-design conditions where the bow shock is not coincident with the cowl lip, there are possible unmodeled effects that could adjust the true mass flow into the engine. These include boundary layer flow and unsteady flexible states changing the bow shock angle and therefore the amount of mass captured by the engine inlet.

5.2.4 Aerodynamic Uncertainty

The aerodynamic models of the hypersonic vehicle model provide a significant source of uncertainty. The aerodynamics encompass all of the pressure distributions over the airframe that produce the lift, drag, and pitching moment of the vehicle. The basis of the aerodynamics of this model is oblique shock and Prandtl-Meyer theory. While these methods can be very accurate for supersonic speeds, uncertainty will be present. Shockwaves at hypersonic speeds get closer to the body, and begin to interact with the boundary layers, creating effects that have not been extensively studied. To simulate this uncertainty, the pressure and temperature after an oblique shock or expansion fan will be treated as uncertain parameters.

Unsteady effects are approximated in this model using first order hypersonic piston theory.[16] The unsteady effects are caused by pitch rates and by structural vibrations. First order hypersonic piston theory is itself an approximation of piston theory since it leaves out higher order effects to simplify calculations. Piston theory itself is an estimation of unsteady forces. Therefore, the modeled unsteady forces may be subject to significant error. The unsteady forces and moments will be treated as uncertain parameters.

5.2.5 Structural Uncertainty

The structure of the vehicle is also be treated as uncertain. Uncertain elements of the structure will be the structural temperature, fuel fraction, pitch mass moment of inertia, and structural damping. The structural temperature is estimated partly by what phase of flight the aircraft is in, whether that is takeoff or hypersonic flight at high altitude. Essentially, the faster the vehicle goes, the higher the structural temperature will be. The structural temperature affects the stiffness of the structure, which influences the natural frequencies of the vibrational modes.

The fuel fraction, or measure of how much fuel remains, is also be varied. In this model the total amount of fuel is over half the weight of the vehicle, so varying the fuel ratio has significant effects on the total mass as well as the pitch mass moment of inertia. The pitch mass moment of inertia is calculated from the approximated structure and the amount of fuel remaining. However, even with accurate estimates of the pitch mass moment of inertia, there will likely be uncertainty about its true value.[9] Finally, the structural damping is also treated as uncertain. The nominal value of structural damping in the model is chosen based on standard aircraft wing damping ratios. The list of uncertain parameters is in Table 5.1.

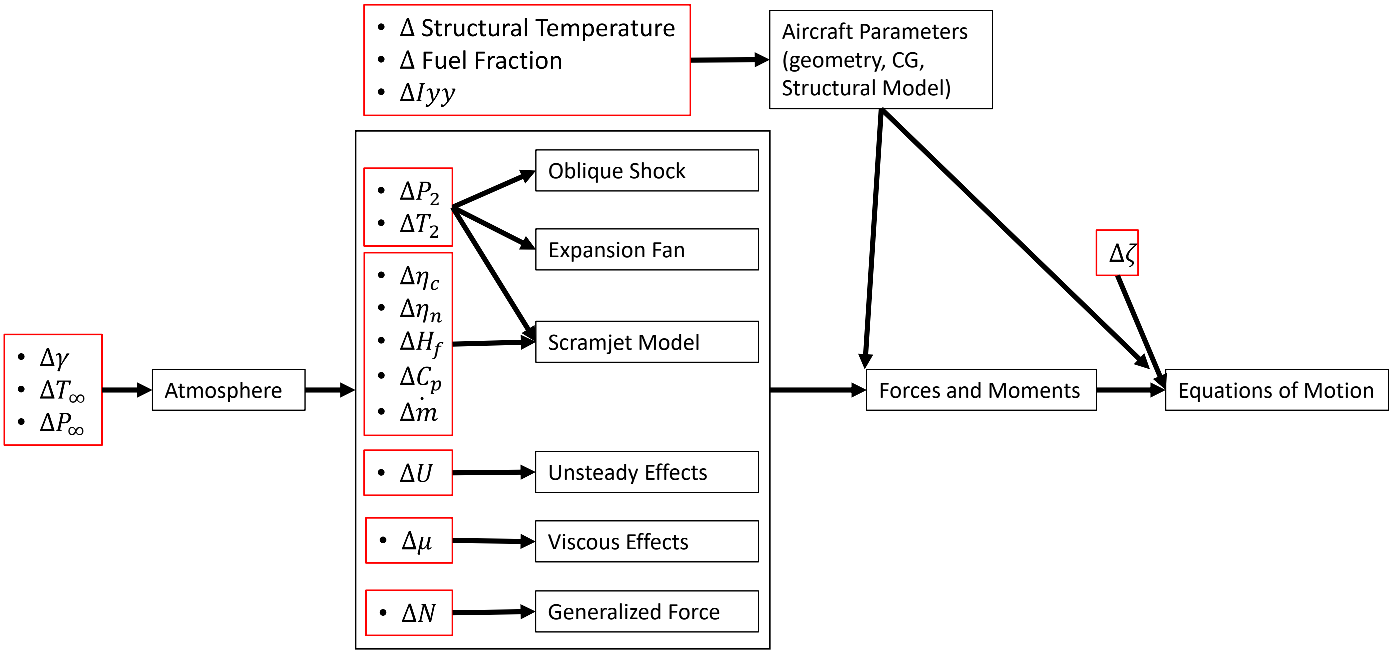

Figure 5.2: Flow of Uncertainty in Matlab Model (Red Denotes Uncertain Input Parameters)

Uncertain Parameter	Uncertainty Distribution
Structural Temperature	Uniform between 480°F and 790°F
Fuel Fraction	Uniform between 0 and 1
Structural Damping Ratio (ζ)	Normal, $\sigma = 20\%$
Pitch Mass Moment of Inertia (Iyy)	Normal, $\sigma = 2\%$
Ratio of Specific Heats (γ)	Normal, $\sigma = 2\%$
Atmospheric Temperature (T_∞)	Normal, $\sigma = 2\%$
Atmospheric Pressure (P_∞)	Normal, $\sigma = 2\%$
Viscosity of Air (μ)	Normal, $\sigma = 2\%$
Specific Heat at Constant Pressure (C_p)	Normal, $\sigma = 2\%$
Combustion efficiency (η_c)	Normal, $\sigma = 2\%$
Nozzle efficiency (η_n)	Normal, $\sigma = 2\%$
Heating Value of H_2 (H_f)	Uniform Between 100% and 105%
Engine Mass Flow ($\dot{m}$)	Normal, $\sigma = 2\%$
Pressure after Oblique Shock (P_2)	Normal, $\sigma = 2\%$
Temperature after Oblique Shock (T_2)	Normal, $\sigma = 2\%$
Pressure after Expansion Fan (P_2)	Normal, $\sigma = 2\%$
Temperature after Expansion Fan (T_2)	Normal, $\sigma = 2\%$
Unsteady Effects (U)	Normal, $\sigma = 5\%$
Generalized Force (N)	Normal, $\sigma = 5\%$

Table 5.1: Uncertain Parameters and Their Distributions. All Standard Deviations are as a Percentage of the Nominal Parameter Value

5.3 Set Up

For this Monte Carlo uncertainty analysis, four cases were considered. Both the original and new control law were tested with the parametric uncertainties as given in Table 5.1. The parametric uncertainties given in Table 5.1 are the smaller or more realistic uncertainties to be experienced. Then, both controllers were tested by increasing the standard deviation of all the normally distributed uncertain parameters to 20% of the nominal value.

For each run, the steady, level, unaccelerated flight (SLUF) trim condition was calculated at the desired Mach and dynamic pressure of $M = 10$ and $\bar{q} = 1500$psf. This flight condition was chosen because it falls in the middle of the flight regime of the vehicle model. The trim condition was found using the $fmincon$ command in Matlab.

After the trim condition was found, the trajectory was simulated for 7 seconds of simulation time. This time frame was chosen because in previous simulations with the control law gains the trajectory had reached a steady state value of flight path angle by 4 seconds. The desired trajectory was to go from a flight angle path angle of 0 deg to 1 deg, while maintaining a desired Mach number of 10.

Each case was run for over 3,000 runs. This provided enough runs to make the Student-T distribution value used in confidence intervals approach that of the normal distribution.

5.4 Results

The trajectories of flight path angle and Mach number were constructed and plotted, with each trajectory having a faint black line, making areas of trajectory concentrations appear darker. For the small uncertainty case, plots are labeled as “Original 2%” and “New 2%”. For the large uncertainty case, the plots are labeled “Original 20%” and “New 20%”. In addition to the trajectory plots, plots of the probability distributions of final flight path angle and Mach number are shown.

5.4.1 Flight Path Angle Results

All the simulated trajectories of the flight path angle are shown in Figure 5.3. For the 2% case, all the trajectories have reached a steady state by 7 seconds. Also, the heavy black area means that the trajectories are very concentrated. The final flight path angle is largely affected by the original rate of change of flight path angle. Trajectories that increase slower than others have a smaller final flight path angle. For the 20% case, the trajectories are a lot more fanned out, with less dark black areas. This indicates greater variability among the trajectories. In addition, not all trajectories have reached a steady value. Some trajectories only decrease in flight path angle. However, the dark core of flight path angles that was seen in the 2% case can still be observed in the 20% case.

The probability distribution of the final flight path angle for the 2% case is shown in Figure 5.4. Interestingly, it appears to not have a normal distribution, but more a uniform distribution. This is likely due to the strong influence of the fuel fraction, which itself was given a uniform distribution. However, what is evident is that the new controller has a lot less variability in system behavior than the original controller. Also evident is that the distribution for the original controller is not centered around 1°.

The 20% case probability distributions are shown in Figure 5.5. Theses distributions look a lot more normal, likely because uncertain parameters besides the fuel fraction have a larger effect on the outcome due to their increased variability. Despite the different shapes of the distributions, the results are similar to the 2% case. The original controller has a greater variability of system behavior than the new controller does, as well as being centered off 1°. The long tails to the right of their peak values could be caused by the fact that the trajectories are still changing and have not reached their steady state value yet. Given a longer simulation time, those tails would likely decrease. The final statistics for all four cases are shown in Table 5.2.

In addition to the probability distributions, The number of trajectories that fall within a given percentage of the desired final value can be calculated. This information is found in Table 5.3. From this, it is obvious that the new controller performs much better than the original controller with regards to flight path angle control.

A linear regression analysis was performed as described previously to study statistical sensitivities. The results of the statistically significant parameters are shown in Table 5.4.

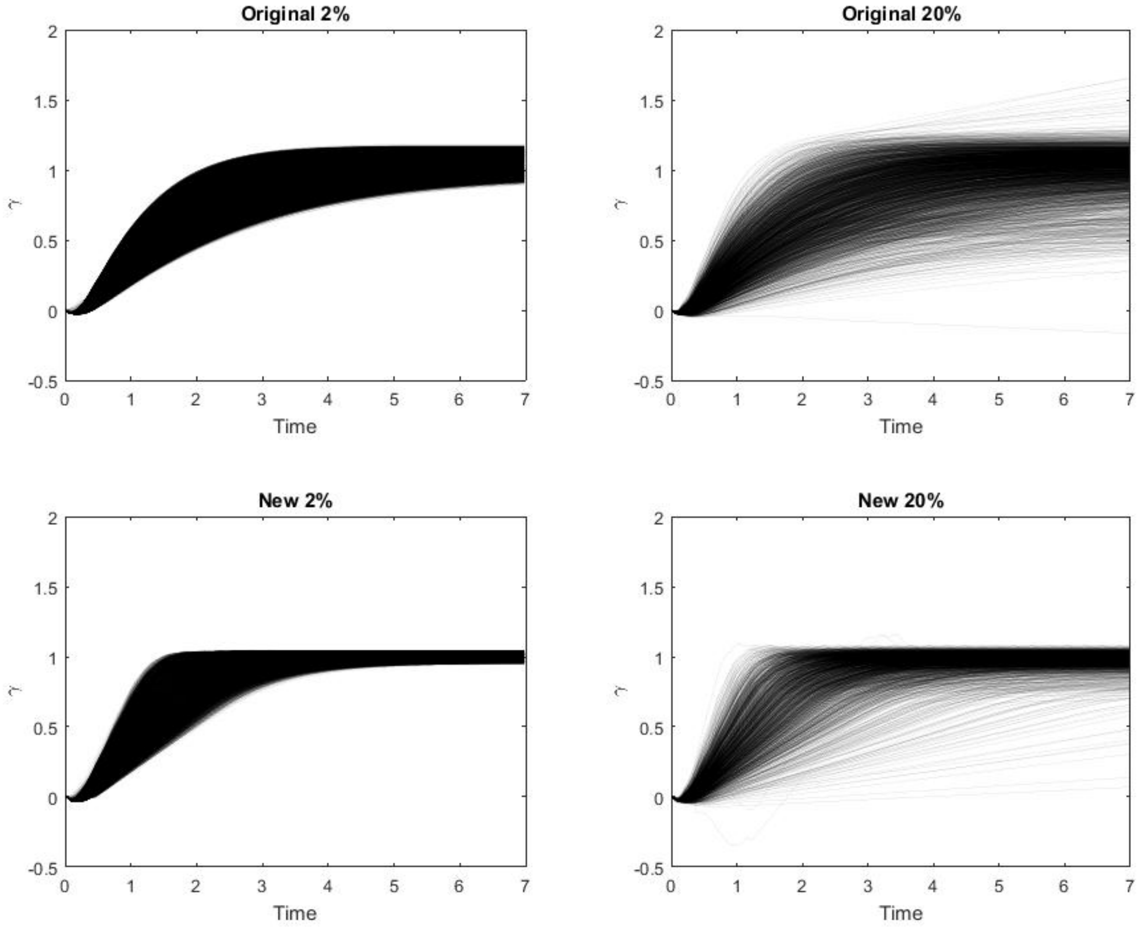

Figure 5.3: Flight Path Angle Trajectories

Not all parameters affected statistically significant results. Uncertain parameters whose 95% confidence interval of the regression coefficient contained zero were declared statistically insignificant, and are not presented. However, fuel fraction, η_c,η_n,P_{2O},T_{2O},T_{2E}, $\dot{m}$ are statistically significant factors affecting the final flight path angle. The fuel fraction has the largest effect on the outcome than any other parameter. This confirms that the more uni-

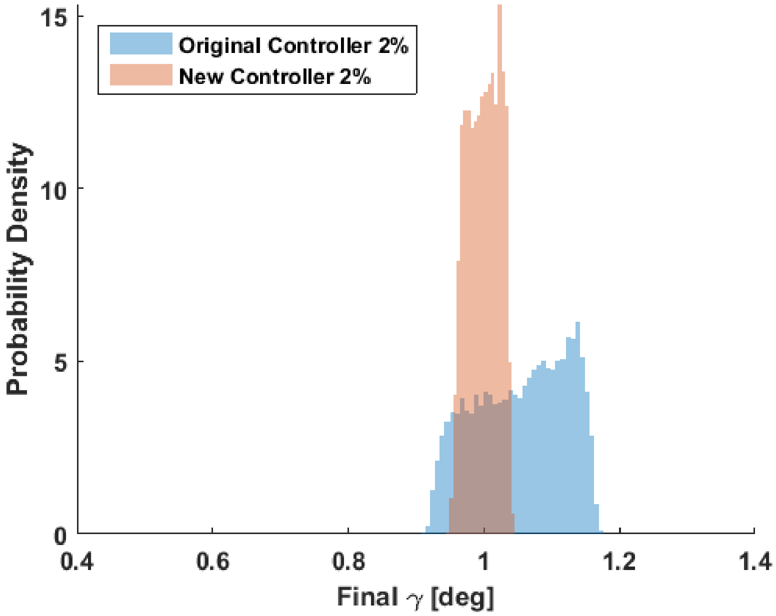

Figure 5.4: Probability Distribution of Final Flight Path Angle Under Small Parametric Deviation

Case	$\bar{x}$	s	95% Confidence
Original 2%σ	1.05°	0.07°	1.048-1.051
New 2%σ	1.00°	0.02°	0.999-1.001
Original 20%σ	0.99°	0.17°	0.984-0.996
New 20%σ	0.97°	0.08°	0.967-0.973

Table 5.2: Final Flight Path Angle Statistics

form distribution of flight path angle in the 2% case is due to the large effect of the uniform fuel fraction distribution. The original controller exhibits larger sensitivities to parameter uncertainties in general, as compared to the new controller. This may also explain why the standard deviation of the final flight path angle was smaller for the new controller.

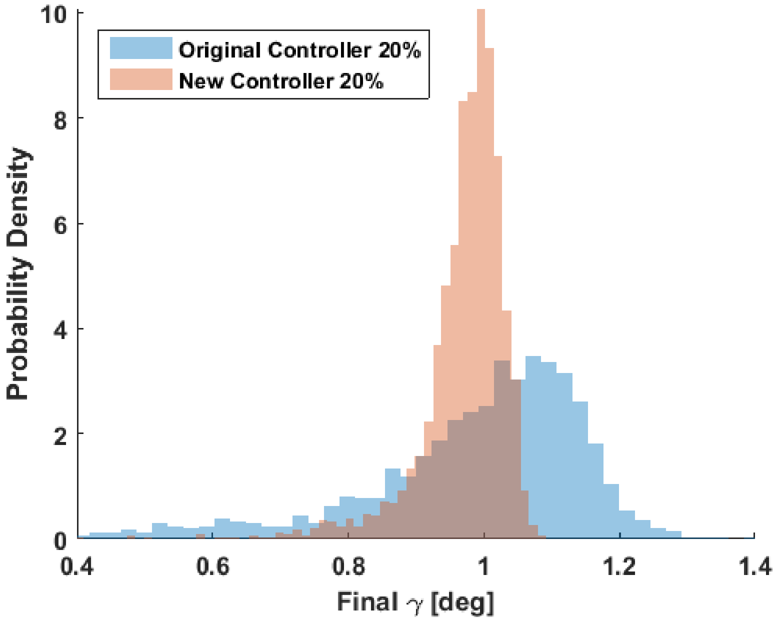

Figure 5.5: Probability Distribution of Final Flight Path Angle Under Large Parametric Deviation

Range from Nominal Trajectory	±5%	±10%	±20%
Original 2% Standard Deviation	47%	89%	100%
Original 20% Standard Deviation	35%	61%	83%
New Controller 2% Standard Deviation	99%	100%	100%
New Controller 20% Standard Deviation	72%	90%	97%

Table 5.3: Percentage of Final γ that Falls within Specified Range from the Nominal Trajectory. Nominal trajectory is trajectory with standard deviation set to zero

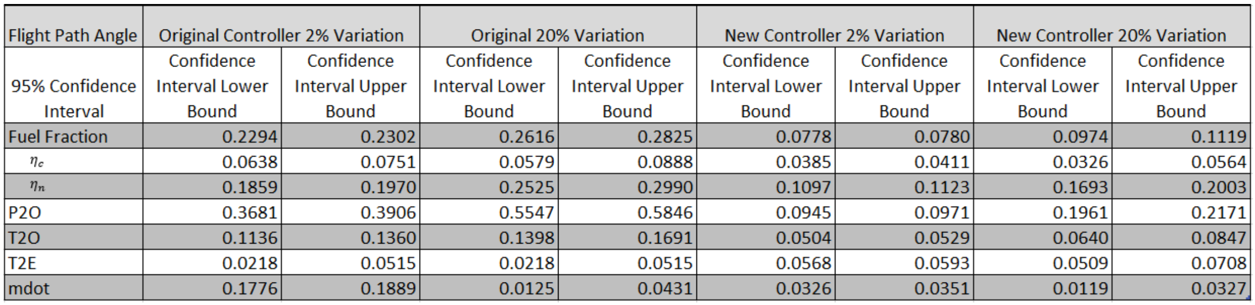

Flight Path Angle	Original Controller 2% Variation		Original 20% Variation		New Controller 2% Variation		New Controller 20% Variation	
95% Confidence Interval	Confidence Interval Lower Bound	Confidence Interval Upper Bound	Confidence Interval Lower Bound	Confidence Interval Upper Bound	Confidence Interval Lower Bound	Confidence Interval Upper Bound	Confidence Interval Lower Bound	Confidence Interval Upper Bound
Fuel Fraction	0.2294	0.2302	0.2616	0.2825	0.0778	0.0780	0.0974	0.1119
η_c	0.0638	0.0751	0.0579	0.0888	0.0385	0.0411	0.0326	0.0564
η_n	0.1859	0.1970	0.2525	0.2990	0.1097	0.1123	0.1693	0.2003
P2O	0.3681	0.3906	0.5547	0.5846	0.0945	0.0971	0.1961	0.2171
T2O	0.1136	0.1360	0.1398	0.1691	0.0504	0.0529	0.0640	0.0847
T2E	0.0218	0.0515	0.0218	0.0515	0.0568	0.0593	0.0509	0.0708
mdot	0.1776	0.1889	0.0125	0.0431	0.0326	0.0351	0.0119	0.0327

Table 5.4: Regression Coefficients: 95% Confidence Intervals of Statistically Significant Uncertain Input Parameters Affecting Final Flight Path Angle

5.4.2 Mach Number Results

All the simulated Mach number trajectories are shown in Figure 5.6. The trajectories of Mach number have not all reached their steady state value, even in the 2% cases. Therefore, the conclusions to be drawn from the Mach number data have less significance than those for the flight path angle.

All Mach trajectories display initial decrease as the angle of attack increases to increase the flight path angle, significantly increasing drag and slowing the hypersonic vehicle. For the new controller in the 2% case, many trajectories reach their steady state desired Mach number of 10. The trajectories for the original controller do not recover to their desired value of 10, but as seen in Figures 5.7 and 5.8, they center around 9.9. The new controller in both figures exhibits a bimodal probability distribution, with one peak at Mach 10 and another slightly less than that. Longer tails are seen in the the 20% case, possibly because they have not reached their steady state value.

The statistics in Table 5.5 reveal that while the new controller leads to a mean closer to the desired Mach number, the variance is larger than the original controller. This could possibly be a tradeoff between flight path angle control and velocity control. Table 5.6 lists the confidence intervals of the linear regression coefficients for the final Mach number. The most important parameter is γ, the ratio of specific heats. In addition, all the scramjet engine uncertain parameters, with the exception of the heating value of H_2, are significant parameters, which is expected. Also, the new controller's linear regression coefficients are larger in magnitude in general than those for the original controller.

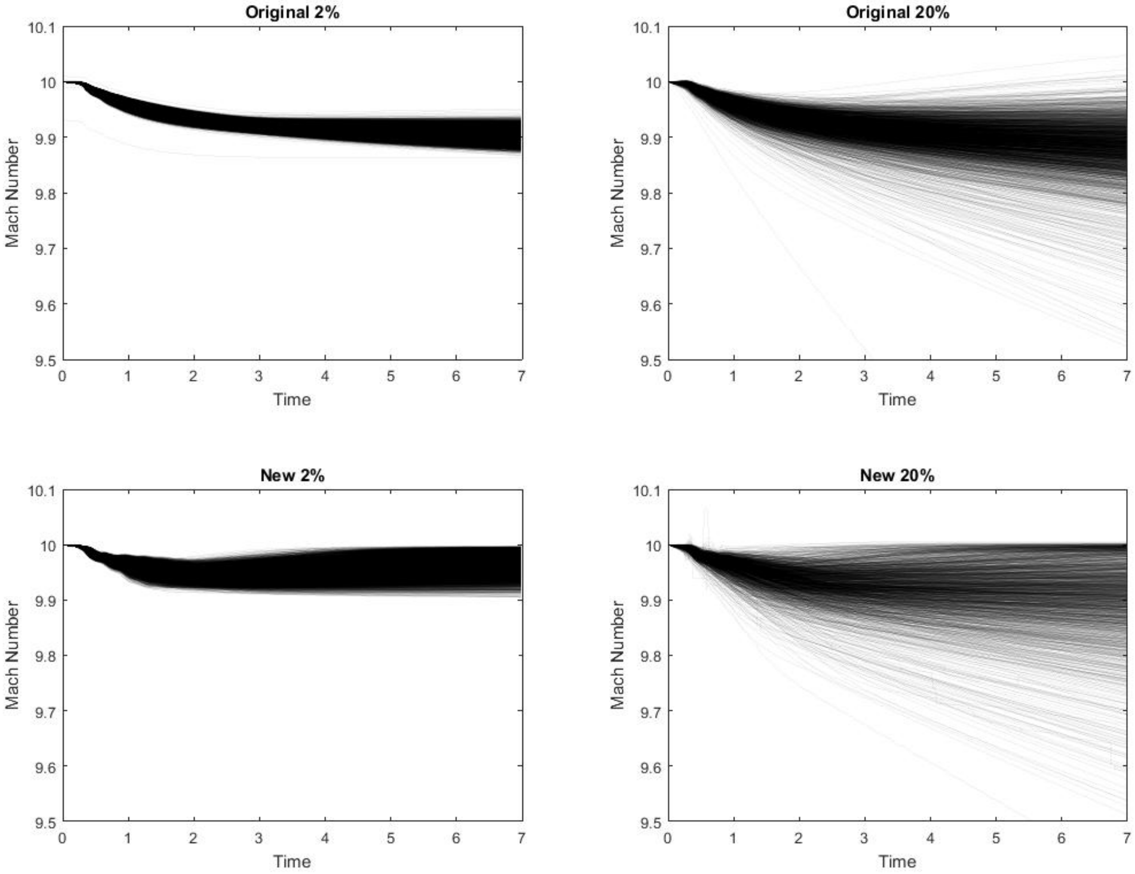

Figure 5.6: Mach Number Trajectories

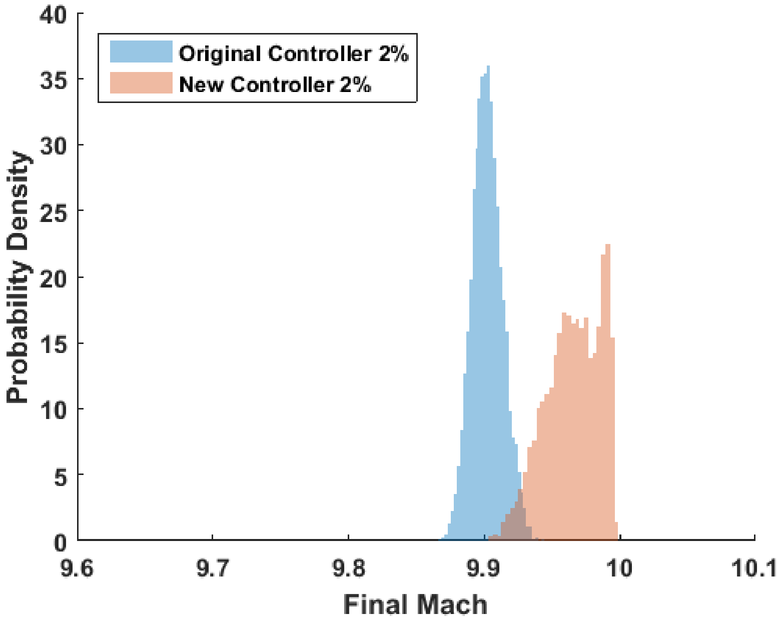

Figure 5.7: Probability Distribution of Final Mach Number Small Parametric Deviation

Case	$\bar{x}$	s	95% Confidence
Original 2%σ	9.90	0.011	9.899-9.900
New 2%σ	9.96	0.020	9.959-9.961
Original 20%σ	9.88	0.059	9.878-9.882
New 20%σ	9.90	0.078	9.897-9.903

Table 5.5: Final Mach Statistics

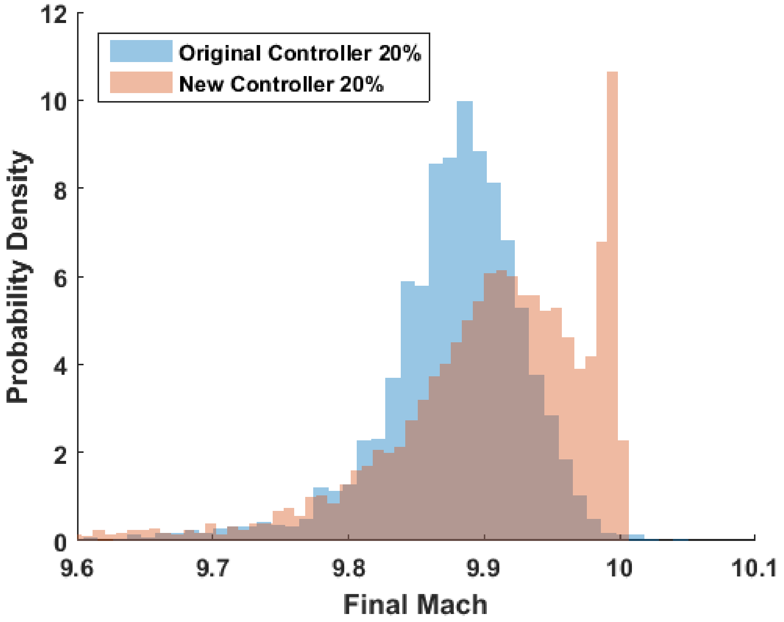

Figure 5.8: Probability Distribution of Final Mach Number Large Parametric Deviation

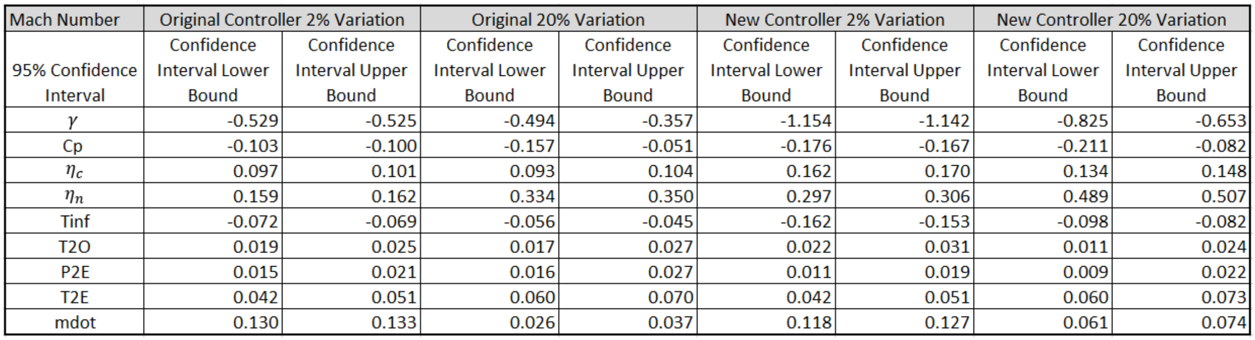

Mach Number	Original Controller 2% Variation		Original 20% Variation		New Controller 2% Variation		New Controller 20% Variation	
95% Confidence Interval	Confidence Interval Lower Bound	Confidence Interval Upper Bound	Confidence Interval Lower Bound	Confidence Interval Upper Bound	Confidence Interval Lower Bound	Confidence Interval Upper Bound	Confidence Interval Lower Bound	Confidence Interval Upper Bound
γ	-0.529	-0.525	-0.494	-0.357	-1.154	-1.142	-0.825	-0.653
Cp	-0.103	-0.100	-0.157	-0.051	-0.176	-0.167	-0.211	-0.082
η_c	0.097	0.101	0.093	0.104	0.162	0.170	0.134	0.148
η_n	0.159	0.162	0.334	0.350	0.297	0.306	0.489	0.507
Tinf	-0.072	-0.069	-0.056	-0.045	-0.162	-0.153	-0.098	-0.082
T2O	0.019	0.025	0.017	0.027	0.022	0.031	0.011	0.024
P2E	0.015	0.021	0.016	0.027	0.011	0.019	0.009	0.022
T2E	0.042	0.051	0.060	0.070	0.042	0.051	0.060	0.073
mdot	0.130	0.133	0.026	0.037	0.118	0.127	0.061	0.074

Table 5.6: Mach Regression Coefficients: 95% Confidence Intervals of Statistically Significant Uncertain Input Parameters Affecting Final Mach Number

Chapter 6

CONCLUSIONS

In this thesis, two different hierarchical control laws for the same air-breathing hypersonic vehicle model were studied: an original one developed in previous work and a new one developed in this work. Monte Carlo simulations were used: first to find the optimal set of control gains that minimized the value of the Lyapunov function derivative in the synthesis of the new control law. Monte Carlo simulations were used again to study the statistical behavior of the actively controlled vehicle subject to uncertainties in all key system parameters. The new control law demonstrated much less sensitivity to parametric uncertainty with respect to flight path angle, but has slightly more variation in Mach number.

Future work should extend the simulation time horizon to gain a better understanding of how the steady state Mach number is affected by the uncertain behavior of the system. Also, given knowledge of how uncertain parameters such as fuel fraction affect the outputs, work should pursue development of techniques, in both modeling and control law synthesis, that would lead to reducing the levels of behavior uncertainty. Long term goals should include extending this work to cases involving hypersonic flight vehicles in their full 3D complexity together with the control technology that they would require.

BIBLIOGRAPHY

[1] Michael A. Bolender and David B. Doman. A nonlinear longitudinal dynamical model of an air-breathing hypersonic vehicle. *Journal of Spacecraft and Rockets*, 22(2):374–381, 2007.

[2] Tom McKenna. Control design for a non-minimum phase hypersonic vehicle model. Master's thesis, University of Washington, 2016.

[3] J.M. Hanson and B.B. Beard. Applying monte carlo simulation to launch vehicle design and requirements analysis. Technical report, NASA, Marshall Space Flight Center, AL, 2010.

[4] Yvonne Gibbs. Past projects: X-43a hypersonic flight program, Aug 2017.

[5] Daryl Meyer. X-51a waverider achieves history in final flight, May 2013.

[6] Frank R. Chavez and David K. Schmidt. Analytical aeroproulsive/aeroelastic hypersonic-vehicle model with dynamic analysis. *Journal of Guidance, Control, and Dynamics*, 17(6), November-December 1994.

[7] Qian Wang and Robert F Stengel. Robust nonlinear control of a hypersonic aircraft. *Journal of Guidance, Control, and Dynamics*, 23(4), 2000.

[8] Harald Buschek and Anthony J Calise. Uncertainty modeling and fixed-order concontrol design for a hypersonic vehicle model. *Journal of Guidance, Control, and Dynamics*, 1997.

[9] Obaid Ur Rehman, Baris Fidan, and Ian Petersen. Uncercainty modeling for robust multivariable control synthesis of hypersonic flight vehicles. In *International Space Planes and Hypersonic Systems and Technology Conference*, 2009.

[10] Kevin P Groves, David O. Sigthorsson, Andrea Serrani, Stephen Yurkovich, Michael A. Bolender, and David B. Doman. Reference command tracking for a linearized model of an air-breathing hypersonic vehicle. In *AIAA Guidance, Navigation, and Control Conference and Exhibit*, 2005.

[11] Lisa Fiorentini, Andrea Serrani, Michael A. Bolender, and David B. Doman. Nonlinear robust adaptive control of flexible air-breathing hypersonic vehicles. *Journal of Guidance, Control, and Dynamics*, 2009.

[12] Samik Raychaudhuri. Introduction to monte carlo simulation. In *Winter Simulation Conference*, 2008.

[13] Gerrit Schutte and Stephan Staudacher. Probabilistic aspects of scramjet design. *Journal of Propulsion and Power*, 25(2), 2009.

[14] Michael W. Oppenheimer, David B. Doman, Jack McNamara, and Adam J. Culler. Viscouse effects for a hypersonic vehicle model. In *AIAA Atmospheric Flight Mechanics Conference*, 2008.

[15] John David Anderson. *Hypersonic and high temperature gas dynamics*. AIAA, 2000.

[16] Michael W. Oppenheimer, David B. Doman, Michael A. Bolender, and Torstens Skujins. A flexible hypersonic vehicle model developed with piston theory. In *AIAA Atmospheric Flight Mechanics Conference*, 2007.

[17] Rudolph J. Swigart. Real-gas hypersonic blunt-body flows. *AIAA Journal*, 1963.

[18] The greenhouse gases, regulated emissions, and energy use in transportation model, greet 1.8d.1. Technical report, Argonne National Laboratories, 2010.

[19] Goro Masuya, Tomokazu Uemoto, Yoshihiro Wakana, Kenji Kudou, Atsuo Murakami, and Tomoyuki Komuro. Performance evaluation of scramjet combustors using kinetic energy and combustion efficiencies. *Journal of Propulsion and Power*, 1999.

[20] Anshu Narang-Siddarth and John Valasek. *Nonlinear Time Scale Systems in Standard and Nonstandard Forms: Analysis and Control*. Society for Industrial and Applied Mathematics, 2014.

Appendix A

CONTROL DESIGN MODEL

Table A.1: Groupings of Curve-Fit Terms.

Definition	Curve-Fit Terms
l_0	$C_L^0 + C_L^\alpha \alpha + C_L^{\eta_1}\eta_1 + C_L^{\eta_2}\eta_2 + C_L^{\eta_3}\eta_3$
l_1	$C_L^{\delta_e}$
d_0	$C_D^0 + C_D^{\alpha^2}\alpha^2 + C_D^\alpha \alpha + C_D^{\eta_1}\eta_1 + C_D^{\eta_2}\eta_2 + C_D^{\eta_3}\eta_3$
d_1	$C_D^{\delta_e}$
d_2	$C_D^{\delta_e^2}$
m_0	$C_M^0 + C_M^{\alpha^2}\alpha^2 + C_M^\alpha \alpha + C_M^{\eta_1}\eta_1 + C_M^{\eta_2}\eta_2 + C_M^{\eta_3}\eta_3$
m_1	$C_M^{\delta_e}$
t_0	$C_T^0 + C_T^{\alpha^3}\alpha^3 + C_T^{\alpha^2}\alpha^2 + C_T^\alpha \alpha + C_T^{\eta_1}\eta_1 + C_T^{\eta_2}\eta_2 + C_T^{\eta_3}\eta_3$
t_1	$C_T^{\alpha^3\phi}\alpha^3 + C_T^{\alpha^2\phi}\alpha^2 + C_T^{\alpha\phi}\alpha + C_T^\phi$

$$c_0 = \frac{\rho M^2 v_s S}{2m}(t_0 \cos\alpha - d_0) = \frac{\bar{q}S}{m v_s}(t_0 \cos\alpha - d_0) \tag{A.1}$$

$$c_1 = \frac{\rho M^2 v_s S}{2m} t_1 = \frac{\bar{q}S}{m v_s} t_1 \tag{A.2}$$

$$c_2 = \frac{\rho M^2 v_s S}{2m} d_1 = \frac{\bar{q}S}{m v_s} d_1 \tag{A.3}$$

$$c_3 = \frac{\rho M^2 v_s S}{2m} d_2 = \frac{\bar{q}S}{m v_s} d_2 \tag{A.4}$$

$$c_4 = \frac{g}{v_s} \tag{A.5}$$

$$c_5 = \frac{\rho M v_s S}{2m}(t_0 sin\alpha + l_0) = \frac{\bar{q}S}{m M v_s}(t_0 sin\alpha + l_0) \tag{A.6}$$

$$c_6 = \frac{\rho M v_s S}{2m} l_1 = \frac{\bar{q}S}{m M v_s} l_1 \tag{A.7}$$

$$c_7 = \frac{v_s}{r} \tag{A.8}$$

$$c_8 = \frac{\rho M^2 v_s^2 S}{2 I_{yy}}(z_T t_0 + \bar{c} m_0) = \frac{\bar{q}S}{I_{yy}}(z_T t_0 + \bar{c} m_0) \tag{A.9}$$

$$c_9 = \frac{\rho M^2 v_s^2 S}{2 I_{yy}} z_T t_1 = \frac{\bar{q}S}{I_{yy}} z_T t_1 \tag{A.10}$$

$$c_{10} = \frac{\rho M^2 v_s^2 S}{2 I_{yy}} \bar{c} m_1 = \frac{\bar{q}S}{I_{yy}} \bar{c} m_1 \tag{A.11}$$

*Note - Eqn A.6 has been corrected from the original work. Sign error.